STIP1/HOP Promotes the Formation of Cytotoxic α-Synuclein Oligomers

Benjamin S. Rutledge[1], Carter J. Wilson[2,3], Rachel M. Lau[1,4], Juan C. Jurado-Coronel[5], Esther del Cid-Pellitero[6], Mikko Karttunen[7,8,9,10], Thomas M. Durcan[6], Edward A. Fon[6], Marco A.M. Prado[5,11], Justin Legleiter[12]*, Martin L. Duennwald[5]* and Wing-Yiu Choy[1]*

[1]Department of Biochemistry, The University of Western Ontario, London, ON, Canada

[2]Computational Biomolecular Dynamics Group, Max Planck Institute for Multidisciplinary Sciences, Göttingen, Germany

[3]Department of Mathematics, The University of Western Ontario, London, ON, Canada

[4]Institute of Biomedical Engineering, University of Toronto, Toronto, ON, Canada

[5]Department of Anatomy & Cell Biology, The University of Western Ontario, London, ON, Canada

[6]Early Drug Discovery Unit, Montreal Neurological Institute-Hospital, McGill University, McGill Parkinson Program, Neurodegenerative Diseases Group, Department of Neurology and Neurosurgery, Montreal Neurological Institute, McGill University, Montreal, QC, Canada

[7]Department of Chemistry, The University of Western Ontario, London, ON, Canada

[8]Department of Physics and Astronomy, The University of Western Ontario, London, ON, Canada

[9]European Laboratory for Learning and Intelligent Systems (ELLIS) Institute Finland, Maarintie 8, 02150 Espoo, Finland

[10]Department of Technical Physics, University of Eastern Finland, P.O. Box 1627, FI-70211 Kuopio, Finland

[11]Robarts Research Institute, Program in Neuroscience, Department of Physiology and Pharmacology, The University of Western Ontario, London, ON, Canada

[12]Department of Biochemistry & Molecular Biology, University of Nevada, Reno, USA

To whom correspondence may be addressed*:

Dr. Wing-Yiu Choy Email: jchoy4@uwo.ca

Dr. Martin Duennwald Email: martin.duennwald@schulich.uwo.ca

Dr. Justin Legleiter Email: jlegleiter@unr.edu

Classification: Biological Sciences - Biochemistry

Keywords: Alpha-synuclein; synucleinopathy; chaperones; protein homeostasis; Stress inducible phosphoprotein 1; Hsp-organizing protein; protein misfolding; protein aggregation; protein fibril; neurotoxicity.

Abstract

The accumulation of alpha-synuclein (a-Syn) as toxic oligomers, and subsequently in Lewy bodies, is a pathological hallmark of Parkinson's disease (PD) and other synucleinopathies. Molecular chaperones and co-chaperones are expected to act in concert to maintain physiological activities of proteins, including a-Syn, but in neurodegeneration this process can become mal-adaptive. Transcript levels of Stress inducible phosphoprotein 1 (STIP1), a co-chaperone of Hsp90/Hsp70, are elevated in brain samples from PD patients. In synucleinopathy mouse models, STIP1 has unexpected bidirectional effects on a-Syn, with overexpression of STIP1 aggravating a-Syn toxicity, whereas knockdown of STIP1 improves toxicity and behavioural phenotypes. However, it is unclear how STIP1 enhances the toxicity of a-Syn. Here we unravel the mechanisms by which the direct interaction between STIP1/HOP and a-Syn regulates the neurotoxicity of a-Syn. Specifically, two binding motifs in the C-terminus of a-Syn directly interact with the TPR2A domain of STIP1/HOP in a dynamic manner, competing for a shared interface on TPR2A. Binding of STIP1/HOP to a-Syn attenuates the formation of a-Syn fibrils while promoting the accumulation of high molecular weight amorphous a-Syn species. Samples of a-Syn aggregated in the presence of STIP1/HOP contain significantly more A11-positive oligomeric species and cause a greater reduction in cell viability than a-Syn aggregated in the absence of STIP1/HOP in neuronal cells. Our results provide a mechanism by which the direct interaction between STIP1/HOP and the C-terminus of a-Syn promotes the formation of cytotoxic, non-amyloidogenic, high molecular weight a-Syn species. Our model offers an explanation for the unexpected pathological link between STIP1 and a-Syn toxicity, thus opening new therapeutic avenues for the treatment of synucleinopathies.

57 ## Introduction

58 The aggregation of alpha-synuclein (a-Syn), a presynaptic neuronal protein, and its
59 deposition in Lewy bodies is a hallmark of Lewy Body Dementia (LBD), Parkinson's disease
60 (PD) and other synucleinopathies [1–3]. a-Syn consists of three domains: an amphipathic N-
61 terminus, the aggregation-prone central non-Aβ component (NAC), and an acidic C-terminus [4].
62 Due to its lack of stable structural elements, a-Syn can be categorized as an intrinsically
63 disordered protein (IDP), which samples an ensemble of diverse conformations. Under
64 pathological conditions, a-Syn is susceptible to adopting conformations that expose its NAC
65 domain, facilitating the formation of toxic polymorphic oligomers and, subsequently,
66 intracellular inclusions of fibrillar a-Syn [5]. Although aggregation has previously been
67 attributed to the NAC region, recent studies indicate that the terminal domains of a-Syn can
68 mediate oligomerization, aggregation, and pathology [6–10]. Accordingly, the N-terminal
69 domain and adjacent residues of a-Syn are central for the neurotoxicity associated with a-Syn
70 oligomers and contain the majority of PD-associated mutations, such as A18T, A29S, A30P,
71 E46K, G51D, A53T, and E83Q [6,11–16]. The C-terminal domain, on the other hand,
72 contributes substantially to the energetic barriers that regulate the transition between monomeric,
73 oligomeric, and fibrillar conformers of a-Syn [17–19].

74 Numerous cellular protein quality control (proteostasis) pathways, such as molecular
75 chaperones and the ubiquitin-proteosome system, participate in modulating a-Syn accumulation
76 and toxicity [20–22]. For instance, up to 90% of a-Syn in live cells is estimated to be engaged in
77 interactions with molecular chaperones [23]. The N-terminus of a-Syn, together with a
78 hydrophobic region around Tyr39, dictates the specificity of the interactions between a-Syn and
79 multiple molecular chaperones [23]. Chaperone binding modulates a-Syn aggregation often

80 through an ATP-independent mechanism, as opposed to the ATP-dependent folding of many
81 other client proteins [24]. Two major cytosolic chaperones, Hsp90 and Hsp70, interact with and
82 shield hydrophobic residues in the N-terminal and NAC regions exposed in non-native
83 aggregation-prone conformers of a-Syn [25–29], thereby inhibiting a-Syn fibrillization and
84 favouring monomeric non-toxic soluble a-Syn conformers *in vitro* [26–28,30]. By contrast, only
85 few interactions mediated by the C-terminal domain of a-Syn have been described, including
86 interactions with calcium [31], tau [32], fatty acid binding protein 3 (FABP3) [33], and the prion
87 protein (PrP^C) [34,35]. As opposed to N-terminal interactions with chaperones such as Hsp90
88 and Hsp70, these described C-terminal interactions appear to promote a-Syn oligomerization and
89 enhance a-Syn toxicity [31–33,36,37].

90 Stress inducible phosphoprotein 1 (STIP1), also known as Hsp-organizing protein (HOP)
91 in humans, is a major co-chaperone to both Hsp90 and Hsp70, facilitating the transfer of client
92 proteins between these two chaperones and regulating their ATPase activity [38–40]. STIP1
93 contains three tetratricopeptide repeat (TPR) domains (TPR1, TPR2A, and TPR2B) and two
94 aspartate and proline rich (DP) domains (DP1 and DP2). STIP1 interacts with Hsp90 via its
95 TPR2A domain and with Hsp70 through its TPR1 and TPR2B domains [39–42]. Although
96 largely known for its role as a Hsp70 and Hsp90 co-chaperone, STIP1 also regulates other
97 proteostatic functions, including proteasomal degradation [43,44], actin dynamics [45], and
98 support of kinase activity [46]. STIP1 can also be secreted into the extracellular space [47,48],
99 where it functions in cell signaling [49].

100 STIP1 has complex effects on several neurodegeneration-associated proteins, including
101 TAR DNA-binding protein 43 (TDP-43) [50], PrP^C [51], amyloid-β [52], and a-Syn [36].
102 Transcript levels of STIP1 are elevated in brain samples from PD patients as compared to

103 healthy individuals [36]. Experiments in a synucleinopathy mouse model indicate that increased
104 levels of STIP1 exacerbate a-Syn aggregation, increase pS129 a-Syn (phosphorylated at serine
105 129) levels, and enhance neurotoxicity. Conversely, decreased levels of STIP1 partially inhibit a-
106 Syn aggregation, reduce the levels of pS129 a-Syn, and mitigate behavioral defects [36],
107 suggesting a dose-dependent relationship between STIP1 function and a-Syn toxicity. STIP1
108 associates with human a-Syn in mouse brains, with the TPR2A domain of STIP1 interacting
109 directly with the C-terminus of a-Syn [36]. However, the mechanism by which STIP1 modulates
110 a-Syn toxicity are still enigmatic.

111 In the present work, we reveal the dynamic interaction between the TPR2A domain of
112 STIP1/HOP and two motifs of negatively charged residues in the C-terminus of a-Syn. We find
113 that this interaction stabilizes soluble, amorphous non-fibrillar conformers of a-Syn, while
114 diminishing the formation of larger a-Syn fibrils. Remarkably, the amorphous non-fibrillar
115 species resemble pathological a-Syn oligomers and are highly toxic to cells. Our study uncovers
116 the molecular mechanisms by which STIP1/HOP interactions favour a toxic oligomeric state of
117 a-Syn. We propose an unexpected pathological link between detrimental proteostasis functions
118 of STIP1 and a-Syn toxicity as a mechanism that can be targeted in synucleinopathies.

119

120 Materials and Methods

121 Peptides derived from the amino acid sequence of a-Syn (a-Syn 110-140: Ac-
122 EGILEDMPVDPDNEAYEMPSEEGYQDYEPEA-COOH; Biotin – a-Syn 110-140: Biotin-
123 EGILEDMPVDPDNEAYEMPSEEGYQDYEPEA-COOH; pS129 a-Syn 110-140: Ac-
124 EGILEDMPVDPDNEAYEMP[pS]EEGYQDYEPEA-COOH; S1: Ac-PVDPDNEAYEM-NH_2,

125 S2: Ac-EEGYQDYEPEA-COOH) and the Hsp90 pentapeptide (Ac-MEEVD-COOH) were
126 synthesized by Tufts University Core Facility. Peptides were dissolved in 40% 20 mM HEPES
127 and 50 mM NaCl at pH 7.2 and 60% 0.1 M ammonium bicarbonate. After dissolving, peptides
128 were dialysed using 1 mL 100-500 Da MWCO dialysis cassettes into 20 mM HEPES and 50 mM
129 NaCl at pH 7.2. Final concentrations were confirmed by amino acid analysis (SPARC BioCentre,
130 The Hospital for Sick Children, Toronto).
131

132 **Recombinant Protein Purification**

133 Human wild type a-Syn and a-Syn mutants (A53T, E137A, D119A/D121A,
134 D135A/E137A/E139A, and D119A/D121A/D135A/E137A/E139A) generated using
135 QuikChange Multi Site-Directed Mutagenesis (Agilent Technologies) were expressed in *E. coli*
136 BL21 (DE3) cells in minimal M9 media containing either $^{14}NH_4Cl$ (1 g/L) or $^{15}NH_4Cl$ (1 g/L) as
137 the sole nitrogen source. Recombinant human a-Syn and mutational variant expression and
138 purification was performed as previously described [36]. All NMR and aggregation kinetics
139 studies were conducted immediately following the purification of a-Syn to avoid any potential
140 influence of storage at -80 °C.

141 pDEST17 (Invitrogen, Carlsbad, CA, USA) expression plasmids encoding full-length
142 mouse STIP1, TPR1 domain (mTPR1; residues 1–118), TPR2A domain (mTPR2A; residues
143 217–352), and the TPR2A domain of human HOP (hTPR2A; residues 217–352) fused with N-
144 terminal tobacco etch virus (TEV) cleavable hexa-His tags were transformed into BL21 (DE3)
145 pLysS for protein expression in minimal M9 media containing either $^{14}NH_4Cl$ (1 g/L) or $^{15}NH_4Cl$
146 (1 g/L) as the sole nitrogen source. Expression and purification of full-length STIP1/HOP and
147 the TPR domains were performed as previously described [53].

148 Protein concentrations were determined by measuring absorbance at 280 nm using a
149 NanoDrop spectrophotometer. For all samples used for determining binding kinetics, protein
150 concentrations were further confirmed by amino acid analysis (SPARC BioCentre, The Hospital
151 for Sick Children, Toronto).

152

153 **S129 Phosphorylation of α-synuclein using PLK3**

154 Phosphorylation of a-Syn and A53T a-Syn at S129 was done as previously described
155 [36]. Reactions containing approximately 5 mg of a-Syn, 4 µg of Polo-like kinase 3 (PLK3)
156 (ThermoFisher PV3812), 50 mM HEPES, 10 mM $MgCl_2$, 1 mM EGTA, 1 mM DTT, and 2 mM
157 ATP were incubated overnight at 30 °C. Following incubation, samples were centrifuged at
158 16,000 x g for 15 minutes at 4 °C to remove any aggregates formed during incubation. Samples
159 were exchanged by dialysis overnight using a 5 mL 500-1000 Da MWCO dialysis cassette with
160 20 mM HEPES and 50 mM NaCl at pH 7.2. The protein was concentrated with a 5 kDa MWCO
161 Vivaspin Turbo 4 centrifugal concentrator (Sartorius) to a volume of 1 mL and Lowry protein
162 assay was used to estimate the concentration. Concentrations were later confirmed by amino acid
163 analysis (SPARC BioCentre, The Hospital for Sick Children, Toronto).

164

165 **Solution NMR spectroscopy**

166 NMR experiments were performed on a 600 MHz Varian Inova/Bruker spectrometer
167 equipped with an xyz-gradient triple resonance probe. The ^{1}H-^{15}N HSQC spectra were collected
168 using 128 × 537 complex points in the ^{15}N and ^{1}H dimensions, respectively. Experiments
169 utilizing ^{15}N labeled a-Syn variants were conducted at 10 °C in 20 mM HEPES and 50 mM NaCl

170 at pH 7.2. For experiments utilizing ^{15}N labeled TPR domains, all experiments were conducted at
171 25 °C in 20 mM HEPES and 50 mM NaCl at pH 7.2. NMR data were processed using NMRPipe
172 [54] and analyzed using NMRViewJ [55] software. Chemical shift analyses of titration sets were
173 conducted using the Titration Analysis function in NMRViewJ. Chemical shift perturbations for
174 ^{1}H-^{15}N peaks were calculated following $\Delta\delta = [(\Delta\delta_{1H})^2 + (0.14*\Delta\delta_{15N})^2]^{1/2}$, where $\Delta\delta_{1H}$ and $\Delta\delta_{15N}$
175 are the changes in ^{1}H and ^{15}N chemical shifts (in ppm) upon the addition of binding target [56].

176

177 **Molecular Dynamics Simulations**

178 Initial configurations comprised residues 111-140 of human a-Syn (N-capped with acetyl
179 group) and human TPR2A. 24 semi-extended configurations of α-synuclein were uniformly
180 positioned around TPR2A (PDB: 1ELR). In each case the distance between at least a pair of
181 heavy atoms (one from each protein) was within 1 nm. These configurations were centered in a
182 10 × 10 × 10 nm cubic box and solvated using mTIP3P [57] (the prefix m denotes the
183 CHARMM36 [58] compatible TIP3P water model) or TIP4P-D water [59]. K^+ and Cl^-
184 counterions were added to ensure neutrality.

185 All simulations were performed using the GROMACS [60] software and the
186 CHARMM36m force field [58]. An initial energy minimization was performed using the
187 steepest descents algorithm. The temperature was maintained at 298.15 K using the Parrinello-
188 Donadio-Bussi velocity rescaling method [61] with a coupling time of 1.0 ps, while the pressure
189 was maintained at 1 bar using the Parrinello-Rahman barostat [62] with a coupling time constant
190 of 5.0 ps. The simulation time step was 2.0 fs. The temperature and pressure were chosen to
191 match physiological conditions. Long-range electrostatic interactions were calculated using the

192 Particle-mesh Ewald (PME) method [63] with a Fourier spacing of 0.12 nm and a real-space cut-
193 off of 1.0 nm. Lennard-Jones interactions were force-switched off between 1 nm and 1.2 nm.
194 Bond lengths were constrained using the Parallel LINear Constraint Solver [64]. Simulations
195 were run for 1.8 μs each, this gave 24 simulations with mTIP3P and 24 simulations with TIP4P-
196 D; the latter was included because it produces highly extended disordered ensembles that have
197 been suggested to well represent experimental observations. These were combined into one large
198 trajectory with frames stored every 1 ns.

199

200 **Biolayer Interferometry**

201 An Octet R2 biolayer interferometry instrument (Sartorius) equipped with the Octet BLI
202 Discovery v12.2 and Octet Analysis Studio v12.2 software was used to measure the binding
203 affinities of the a-Syn 110-140, S1, S2, and Hsp90 pentapeptide for hTPR2A. Biotinylated
204 hTPR2A was produced by incubating 15 μM hTPR2A with Biotin-maleimide (Sigma B1267) in
205 20 mM HEPES and 50 mM NaCl at pH 7.2 for 30 minutes at room temperature. After
206 incubation, the sample was buffer exchanged into fresh 20 mM HEPES and 50 mM NaCl at pH
207 7.2 using a 5 kDa MWCO Vivaspin Turbo 4 (Sartorius) concentrator with 4 sample volumes of
208 fresh buffer to remove unreacted biotin-maleimide. Biotinylated hTPR2A or the Biotin-a-Syn
209 110-140 peptide were immobilized onto streptavidin (SA) biosensors (Satorius) by incubating
210 the sensor in 3 μM of biotinylated hTPR2A or the Biotin-a-Syn 110-140 peptide for 10 minutes.
211 The biosensors were then quenched in 1 mM free biotin for 10 minutes to prevent non-specific
212 binding. The biosensors were then dipped into wells of increasing concentrations of ligand for
213 60-120 seconds and dissociation was monitored by dipping the biosensor in 20 mM HEPES and
214 50 mM NaCl at pH 7.2 supplemented with 0.1% BSA and 0.02% Tween 20.

215 The assays were performed using 96 well plates at 25 °C with 1,000 rpm agitation in 20
216 mM HEPES and 50 mM NaCl at pH 7.2 supplemented with 0.1% BSA and 0.02% Tween 20 to
217 prevent non-specific binding. An unloaded SA biosensor was dipped into buffer alone and the
218 subsequent ligand samples as a control. The Biotin-a-Syn 110-140 peptide was immobilized and
219 the binding of hTPR2A was fit to a heterogeneous binding model to calculate the binding
220 affinity. Biotinylated hTPR2A was immobilized to monitor the binding of the Hsp90
221 pentapeptide as well as the a-Syn C-terminal, S1, and S2 a-Syn peptides, all of which were fit to
222 a one-to-one binding model to determine binding affinity.

223

224 **ThT aggregation assays**

225 For all aggregation experiments, wild type a-Syn was used unless stated otherwise.
226 Thioflavin T (ThT) dye was used at a final concentration of 10 μM to monitor the aggregation of
227 a-Syn (concentrations ranging from 20 μM to 60 μM based on experimental design) using the
228 excitation wavelength of 445 nm and emission wavelength of 485 nm. Samples contained wild
229 type or variant a-Syn with the absence or presence of various concentrations of the TPR domains
230 and in the absence or presence of peptides. The reaction buffer consisted of phosphate buffer
231 saline (PBS) at pH 7.4 with 0.1% sodium azide to prevent bacterial growth. For delayed addition
232 of hTPR2A, concentrated hTPR2A (>1.5 mM) was added at equimolar concentration to a-Syn
233 directly into the well for each sample at its corresponding time point to avoid significant volume
234 changes. Each experiment was performed with 4 replicates and values were averaged. Each
235 replicate consisted of a 50 μL final reaction volume and replicates were monitored in black non-
236 binding half volume 96-well plates with clear bottoms (Corning Incorporated). A sterile glass
237 bead (~2.7 mm diameter) was added to each well to aid with sample mixing. A Cytation 5 Cell

238 Imaging Multi-Mode Reader (Biotek, Winnoski, VT, USA) was used at a temperature of 37 °C
239 with continuous orbital shaking at 425 rpm.

240

241 **Electron Microscopy**

242 Fibrillar a-Syn samples were produced by aggregating 175 μM a-Syn in the absence or
243 presence of equimolar mTPR1 or hTPR2A for 5 days at 37 °C in a shaking incubator (400 rpm).
244 Samples were characterized using a negative staining. They were added to 200 mesh carbon
245 coated copper grid (3520C-FA, SPI Supplies), fixed with 4% PFA and stained with 2% acetate
246 uranyl (22400-2, EMS) for 1 minute. Aggregated a-Syn samples were visualized using a
247 transmission electron microscope (Tecnai G2 Spirit Twin 120 kV Cryo-TEM) coupled to a
248 camera (Gatan Ultrascan 4000 4 k × 4 k CCD Camera System Model 895) and analyzed with
249 Fiji-ImageJ1.5 and GraphPad Prism 9 software.

250

251 **Size exclusion chromatography**

252 a-Syn at a concentration of 300 μM was incubated in the absence and presence of
253 hTPR2A at an equimolar concentration in 20 mM HEPES and 50 mM NaCl at 37 °C with a
254 shaking speed of 400 rpm. A sterile glass bead (~2.7 mm diameter) was added to each sample to
255 aid with mixing. To ensure that hTPR2A did not form high molecular weight species itself, a
256 control sample of 300 μM hTPR2A was subjected to the same aggregation conditions. All
257 samples were run on a Superdex 200 Increase 10/300 GL (Cytiva) column with a flow rate of 0.6
258 mL/min. Elution was collected and analyzed by SDS-PAGE using Coomassie Blue stain.

259

260 **Atomic Force Microscopy**

261 The a-Syn, mTPR1, and hTPR2A mixtures were prepared in the same manner as for
262 other ThT assays. To remove any possible contaminants, protein stocks were filtered using a 0.8
263 μM syringe filter before preparing the mixtures. Incubations of a-Syn alone and with equimolar
264 amounts of mTPR1 or hTPR2A were shaken at 400 rpm on an orbital shaker, and each
265 incubation contained a sterile glass bead (~2.7 mm diameter). At various time points, 2 μL
266 aliquots of each condition were taken and deposited on freshly cleaved mica, allowed to sit on
267 the substrate for 1 min, were then washed with 100 μL of 18 MΩ water, and dried with a gentle
268 stream of nitrogen. Imaging of samples was performed on a Nanoscope V Multimode Atomic
269 Force Microscope (AFM) (Veeco, Santa Barbara, CA) with a closed-loop vertical engage J-
270 scanner. All images were obtained in tapping mode utilizing a diving-board-shaped silicon oxide
271 cantilever with a spring constant of 40 N/m and the resonance frequency of ~300 kHz.

272 AFM image processing and analysis was performed in Matlab (MathWorks, Natick, MA)
273 by utilizing the imaging processing toolbox as previously described [65]. A 2nd order polynomial
274 flattening algorithm was used to correct for background curvature. A height threshold (z = 0.9
275 nm) was implemented to produce binary maps used to identify discreet aggregates in each image.
276 Physical features of individual aggregates (e.g., height, volume, diameter, and area covered)
277 were measured. Each aggregate was also assigned a tracking number. A minimum of five 5 × 5
278 μm AFM images for each time point was analyzed, resulting in a minimum of 125 μm^2 of
279 surface area analyzed. As fibrils and fibril bundles are typically larger and demonstrate an
280 elongated morphology relative to oligomers and amorphous aggregates, data sets were filtered
281 for a minimum area occupied by the aggregate (75 pixels) and aspect ratio (> 2) to identify fibrils

282 and determine fibril load. The reliability of these filters to correctly identify fibrils was validated
283 by labeling the aggregates that passed the filters directly in the images. Aggregates that did not
284 pass the morphological filters were categorized as oligomers or amorphous aggregates.

285

286 **Dynamic Light Scattering**

287 Samples from a ThT assay conducted using 20 μM a-Syn in the absence and presence of
288 equimolar hTPR2A were collected after 3 and 6 days of aggregation. Samples were pulse spun
289 briefly before dynamic light scattering measurements. The upper portion of the sample was used
290 to avoid dust contamination from the sample but maintain high molecular weight species and
291 fibrils. Measurements were done using a Dynapro NanoStar dynamic light scattering instrument
292 (Wyatt Technologies) with an incident light wavelength of 825 nm and a scattering angle of 90°.
293 For each sample, 20 consecutive autocorrelation functions, each with a 5 second accumulation
294 time were acquired and the autocorrelation functions of the 10 lowest scattering acquisitions
295 were averaged for hydrodynamic size calculations. Deconvolution was performed using the
296 accompanying DYNAMICS software (v7.1.9) between 1.5 μs and 100 ms for all averaged
297 curves using identical resolution settings for each sample. All calculations used a solvent index
298 of 1.333 and a viscosity of 1.019 $g\ m^{-1}\ s^{-1}$.

299

300 **Dot Blot Assay**

301 The a-Syn (70 μM) aggregation reactions in PBS buffer were incubated at 37 °C in a
302 shaking incubator (500 rpm) in the presence or absence of equimolar hTPR2A for 1, 2, 3, 5, or 7
303 days to induce aggregation. Aggregation reactions were run in triplicate for each time point. For

304 each time point, the sample was diluted to a final concentration of 15 μM, 3 μM, and 0.6 μM. A
305 nitrocellulose membrane was pre-wet by soaking it in PBS for 5 minutes before placing it in a
306 Minifold I Dot-Blot 96-Well System (10447900, VWR) and applying vacuum. Each well was
307 washed with 100 μL of PBS using low vacuum. For each dilution of the aggregation samples, 10
308 μL was blotted on the membrane using low vacuum and the membrane was allowed to dry. The
309 membrane was then blocked using 5% skim milk powder (Carnation/Nestle,
310 Vevey, Switzerland) in Tris-buffered saline with 0.05% (v/v) Tween 20 (Thermo Fisher
311 Scientific, Waltham, MA, USA) (TBST) and incubated for 1 hour on a shaker at room
312 temperature. Following blocking, the membrane was washed with 10 mL aliquots of TBST for
313 10-minute intervals over a 30-minute period. The membrane was then incubated overnight with
314 primary A11 antibody (Invitrogen, Carlsbad, CA, USA, AHB0052) diluted in TBST with 5%
315 (w/v) Bovine serum albumin (BSA) (Wisent Inc, Quebec, Canada) on a shaking incubator at 4
316 ºC. The membrane was washed again using 10 mL aliquots of TBST at 10-minute intervals for
317 30 minutes and then incubated in Rabbit secondary antibody conjugated with Alexa680 diluted
318 in TBST with 1% (w/v) BSA on a shaker for 1 hour at room temperature. Following incubation,
319 the membrane was washed in 10 mL of TBST and the membrane was imaged using the
320 ChemiDoc MP Imaging System (Bio-Rad, Hercules, CA, USA) and analyzed using Image Lab
321 (Bio-Rad, Hercules, CA, USA).

322

323 **Yeast Strains and Yeast Media**

324 The yeast strain BY 4741 (MAT α his3Δ1 leu2Δ0 lys2Δ0 ura3Δ0) was used in this study.
325 Yeast-peptone-dextrose (YPD)-rich media (10 g/L of yeast extract, 20 g/L of peptone, and 20
326 g/L of dextrose) and selective dextrose (SD) media (6.7 g/L yeast nitrogen base (YNB), 60 mg/L

327 of L-isoleucine, 20 mg/L of L-arginine, 40 mg/L of L-lysine HCl, 60 mg/L of L-phenylalanine,
328 10 mg/L of L-threonine, and 2% glucose) in either liquid media or agar plates (20 g/L) were used
329 to grow yeast cells. SD media was supplemented with four different amino acids (40 mg/L of L-
330 tryptophan, 60 mg/L of L-leucine, 20 mg/L of L-histidine-monohydrate, 10 mg/L of L-
331 methionine, and 20 mg/L of uracil) depending on the selective marker of the plasmid. To expose
332 cells with the established Hsp90 inhibitor, Radicicol, liquid media or plates were supplemented
333 with 10 µg/mL of Radicicol.

334

335 **Yeast Transformations**

336 Yeast transformations were performed utilizing the standard PEG/lithium acetate
337 transformation method [66].

338

339 **Growth Assays (Spotting assays) and Quantification**

340 The relative growth of the yeast cells was measured using spotting assays and
341 quantification as described by Petropavlovskiy et al [67]. In summary, 3 mL of SD media was
342 inoculated with cells and incubated in a shaking incubator at 30 °C overnight. A 48-prong
343 frogger (V&P Scientific, San Diego, CA, USA) was used to spot normalized serial dilutions of
344 cells onto SD plates lacking the selective amino acid. For Radicicol treated plates, Radicicol was
345 added to SD media to a final concentration of 10 µg/mL immediately before media was poured
346 when warm to the touch. Plates were incubated at either 30 °C or 37 °C and growth was
347 monitored during the entire growth period. All spotting assays contain respective control lanes
348 on each experimental plate, and images of the plates were cropped and separated to highlight

349 relative side-by-side comparisons. Unless otherwise indicated, the pixel count of the third
350 dilution of the growth assay was used for quantification. Values were normalized to the average
351 of the respective control lanes. For all growth assays, a minimum of three biological replicates
352 were used.

353

354 **Fluorescent Microscopy and Quantification**

355 SD media was inoculated with yeast expressing fluorescently tagged constructs and
356 incubated overnight at either 30 °C or 37 °C in a shaking incubator. For Radicicol treatment,
357 cultures were treated with 10 μg/ml Radicicol 6 hours prior to imaging. Each culture (1-2 μL)
358 was placed on a microscope slide and imaged using a Zeiss Axio Vert.A1 microscope. For each
359 condition, three biological replicates were imaged, and three images of random fields of each
360 biological replicate were imaged. The extent of a-Syn foci formation was quantified as the
361 percentage of cells that contained a-Syn foci as described by Petroi et al [68]. Each data point
362 represents the average percentage of cells that contained foci across the three images taken for
363 each respective biological replicate. For each biological replicate, a minimum of 100 cells was
364 counted towards the percent of cells containing foci unless otherwise stated.

365

366 **Mammalian cell culture and media**

367 The SH-SY5Y cell line was used in the course of this study. Cells were grown in
368 Dulbecco's Modified Eagle Medium (DMEM, Corning, Corning, NY, USA) with 4.5 g/L
369 glucose. Media was supplemented with 10% fetal bovine serum (FBS, Gibco/Thermo Fisher

370 Scientific, Waltham, MA, USA) and 1X penicillin-streptomycin solution (Corning, Corning, NY,
371 USA). Cells were grown at 37 °C with 5% CO_2.

372

373 **Cytotoxicity Assay**

374 The cytotoxicity assay protocol was adapted from the protocol previously described by
375 Daturpalli et al [26]. Cell viability was measured using the CellTiter-Glo 2.0 Luminescent Cell
376 Viability Assay (Promega, Madison, WI, USA), which determines the number of viable cells in
377 the culture by measuring the amount of available ATP. Cells were split into a 96-well plate and
378 grown for 48 hours at 37 °C DMEM. Each well was seeded with 10,000 cells. The a-Syn (70
379 μM) aggregation reactions in PBS buffer were incubated at 37 °C in a shaking incubator (500
380 rpm) in the presence or absence of equimolar hTPR2A for 1, 2, 3, 5, or 7 days to induce
381 aggregation. Aggregation reactions were run in triplicate for each time point. The cell media was
382 exchanged with culture medium supplemented with aggregation samples. The final concentration
383 of a-Syn in the cell media was 35 μM (calculated using the initial monomer concentration).
384 Controls were mixed containing monomeric a-Syn, hTPR2A, and PBS buffer using the same
385 respective volumes of media and buffer as the aggregation samples. The SH-SY5Y cells were
386 incubated for 16 hours in the treated media. The CellTiter-Glo 2.0 Luminescent Cell Viability
387 Assay was carried out following the supplier's instructions and signal was measured using a
388 Cytation 5 Cell Imaging Multi- Mode Reader (Biotek, Winooski, VT, USA).

389

390 **Statistical analysis**

391 Statistical analysis of ThT assays, Dot blots, cell viability, growth assays, and percentage
392 of foci assessed by microscopy were performed using the GraphPad Prism X software
393 (GraphPad Software, Boston, MA). To determine statistical significance, unpaired t-tests were
394 used to compare means and standard deviations between relevant controls and experimental data
395 sets (each data set was composed of a minimum of 3 biological repeats). The P values are
396 provided for all conditions where $P < 0.05$. Bars represent standard errors of the mean.

397

398 ## Results

399 **Two linear motifs in the C-terminal domain of a-Syn mediate its interaction with the**
400 **TPR2A domain of HOP**

401 Mouse STIP1 shares a high sequence identity (97.4%) with its human homologue (HOP),
402 with only three amino acid positions (residues 243, 250, and 269) differing between STIP1-
403 TPR2A domain (mTPR2A; residues 217–352) and the TPR2A domain of human HOP
404 (hTPR2A). NMR ^{1}H-^{15}N HSQC experiments were used to confirm that hTPR2A interacts with
405 a-Syn in the same manner as mTPR2A [36]. Measuring the changes (perturbations) in the
406 chemical shifts for each assigned residue allows for the identification of the binding interface and
407 insights into the strength of the interaction. Almost identical chemical shift perturbations (CSPs)
408 are observed in C-terminal residues of ^{15}N-labeled a-Syn, pS129 a-Syn, A53T a-Syn, and pS129
409 A53T a-Syn in the presence of mTPR2A and hTPR2A (Figures S1 and S2). Notably, minor
410 CSPs are observed for some residues in the N-terminal domain, likely due to the loss of transient
411 long-range intramolecular interactions between the N- and C-terminal domains of a-Syn upon
412 mTPR2A/hTPR2A binding [69]. These results clearly indicate that, like the mTPR2A domain of
413 STIP1, the hTPR2A of HOP mediates the interaction with the C-terminal domain of wild type
414 and pathological variants of human a-Syn.

415 Next, to identify key residues in the C-terminal domain of a-Syn that regulate the binding
416 of hTPR2A, we acquired ^{1}H-^{15}N HSQC spectra of ^{15}N-labeled a-Syn in the presence of
417 increasing concentrations of hTPR2A. Quantitative analysis of the NMR titration series reveals
418 that two negatively charged residues in the middle of the C-terminal domain (D119 and D121)
419 and three negatively charged residues close to the C-terminus (D135, E137, and E139) display

420 large CSPs upon binding hTPR2A (Figs. 1A, 1B, and 1E). Group fitting the CSPs of these
421 residues to a 1:1 binding model yields a dissociation constant of 169 ± 67 μM for a-Syn/hTPR2A
422 binding. To further assess the contributions of these two groups of acidic residues to hTPR2A
423 binding, we repeated the NMR titration experiment with a D119A/D121A double mutant of a-
424 Syn (Fig. 1C). Notable CSPs were no longer observed for the residues neighbouring the D119A
425 and D121A mutation sites, suggesting D119 and D121 are crucial for hTPR2A binding.
426 Unexpectedly, CSPs observed for D135, E137, and E139 are not substantially reduced,
427 indicating that their interactions with hTPR2A are largely unaffected by the D119A and D121A
428 substitutions (Figs. 1C and 1F). Similarly, D135A, E137A, and E139A substitutions result in no
429 notable CSPs of residues neighbouring the D135A, E137A, and E139A mutation sites upon
430 hTPR2A titration, whereas the CSPs for D119, D121, and neighboring residues were not
431 considerably reduced (Figs. 1D and 1G). Finally, D119A, D121A, D135A, E137A, and E139A
432 substitutions result in no observable CSPs upon the addition of hTPR2A (Fig. 1H). Taken
433 together, these results suggest that the C-terminus of a-Syn contains two motifs that interact
434 independently with hTPR2A, with site 1 (S1) containing the key charged residues D119 and
435 D121 and site 2 (S2) with residues D135, E137 and E139, both of which can bind hTPR2A (Fig.
436 1I).

437

438 **The S1 and S2 motifs compete for binding of overlapping interfaces on hTPR2A**

439 To identify the interfaces on hTPR2A involved in the interaction with the two binding
440 motifs in the C-terminus of a-Syn we performed NMR ^{1}H-^{15}N HSQC experiments on ^{15}N-
441 labeled hTPR2A in the presence of peptides comprising residues 110-140 (C-terminal peptide),
442 residues 117-127 (S1 peptide), and residues 130-140 (S2 peptide) of a-Syn (Figure S3). CSPs

443 were plotted against residue number in hTPR2A and residues experiencing above average CSPs
444 were mapped onto the complex structure of hTPR2A (Figs. 2A-C) [70]. Intriguingly, addition of
445 peptides that cover the C-terminal domain of a-Syn, the S1 motif, and the S2 motif causes CSPs
446 of similar residues within the hTPR2A, indicating that either the S1 or S2 motif alone is
447 sufficient to interact with hTPR2A. Importantly, the results indicate that binding of both S1 and
448 S2 is primarily mediated by the same set of residues in hTPR2A, suggesting that S1 and S2
449 interact with the same interface on hTPR2A. Notably, the C-terminal peptide does not form
450 additional interactions with hTPR2A beyond S1 and S2 (Figs. 2A-C).

451 We conducted competitive binding NMR experiments to confirm that a-Syn peptides
452 compete with full-length a-Syn for binding hTPR2A. We monitored CSPs of ^{15}N-labeled a-Syn
453 in the presence of equimolar hTPR2A upon the addition of C-terminal, S1, or S2 peptide. If the
454 peptides compete with regions of a-Syn for the same binding interface on hTPR2A, the CSPs for
455 those regions of a-Syn are expected to reduce as a larger proportion exists in the unbound state.
456 The addition of equimolar S1 or S2 peptide reduces the CSPs of key residues within both S1
457 (D119 and D121) and S2 (D135, E137 and E139) motifs of full-length a-Syn (Fig. 2E).
458 Furthermore, both S1 or S2 peptides reduce the CSPs of ^{15}N-labeled a-Syn to a lesser extent than
459 the addition of the a-Syn C-terminal peptide or the pS129 a-Syn C-terminal peptide. This
460 suggests that S1 and S2 individually have a lower binding affinity for hTPR2A as compared to
461 peptides that are comprised of both S1 and S2 (Fig. 2E). Taken together, these results show that
462 both S1 and S2 compete for a single binding interface on hTPR2A.

463

464 **The S1 and S2 binding motifs of a-Syn compete for the Hsp90-binding pocket of hTPR2A**

465 The TPR2A domain of STIP1/HOP mediates Hsp90 interactions by binding to its C-
466 terminus [70]. Interestingly, our previous experiments demonstrated that the pentapeptide
467 (MEEVD) comprising the C-terminus of Hsp90 is sufficient to disrupt mTPR2A/a-Syn binding
468 [36]. We demonstrated here that many of the residues within hTPR2A that show CSPs upon
469 binding a-Syn are adjacent to residues essential for its interaction with Hsp90. Upon addition of
470 the Hsp90 pentapeptide, three clusters of residues in hTPR2A showed the largest CSPs,
471 indicating interacting residues (Fig. 2D). Notably, the majority of the residues within these three
472 clusters also show the largest CSPs upon addition of the C-terminal peptide of a-Syn and both
473 the S1 and S2 peptides (Figs. 2A-C). Furthermore, competitive binding NMR experiments reveal
474 that in the presence of equimolar hTPR2A, CSPs for residues in both S1 and S2 of ^{15}N-labeled a-
475 Syn are substantially reduced upon the addition of equimolar Hsp90 pentapeptide (Fig. 2E).
476 Taken together, these results demonstrate that the Hsp90 pentapeptide interacts with the same
477 interface on hTPR2A shared by both S1 and S2 of a-Syn and can displace S1 and S2 upon
478 binding hTPR2A.

479

480 **Computational modelling suggests dynamic binding between a-Syn and hTPR2A**

481 To model the multi-site interactions between a-Syn and hTPR2A, we performed
482 extensive unbiased molecular dynamics (MD) simulations of the C-terminal peptide of a-Syn in
483 the presence of hTPR2A. Global contact analysis suggested the importance of electrostatic
484 interactions and interactions with residues containing aromatic side chains (Fig. 2F). To assess
485 how S1 and S2 of a-Syn differentially interact with hTPR2A, we determined the time-dependent
486 contact propensity of acidic residues in both motifs with positively charged residues in
487 hTPR2A. Performing a principal component analysis (Fig. 2G, inset) we found ~40% of the

488 variance could be described by PC1 which also well separated the propensity for S1 (blue) or
489 S2 (green) to form contacts. Quantifying the nature of these contacts revealed that although S1
490 and S2 can simultaneously bind to hTPR2A, nearly half of the contacts involved exclusively
491 either S1 or S2, with S2 showing a higher propensity for these solo interactions (i.e., ~26% vs.
492 ~16%) (Fig. 2G). Notably, the MD simulations predict that when S1 occupies the Hsp90
493 pentapeptide binding interface on hTPR2A, S2 can still make transient interactions with
494 neighboring charged residues on hTPR2A and vice versa (Movie S1). The average number of
495 total contacts for S1 was 2.34 ± 0.24, while for S2 was 2.63 ± 0.26. Overall, the simulations
496 agree with our NMR findings, underlining the importance of electrostatic interactions in
497 facilitating a-Syn/hTPR2A binding. The NMR analyses and MD simulations together suggest a
498 dynamic binding mechanism between a-Syn and hTPR2A via the S1 and S2 motifs of a-Syn
499 (Fig. 2H).

500

501 **Competitive two-site binding enhances the affinity of a-Syn for hTPR2A**

502 The C-terminal a-Syn peptide was significantly more effective than the S1 and S2
503 peptides in competing with the full-length a-Syn for binding to hTPR2A. This suggests that
504 multivalent interactions between the S1 and S2 motifs of a-Syn and hTPR2A increase the overall
505 affinity of binding through avidity effects [71]. We employed Bio-Layer Interferometry (BLI) to
506 determine the binding affinities of different a-Syn peptides for immobilized hTPR2A (Figure
507 S4). The global binding affinity between hTPR2A and the C-terminal a-Syn peptide was
508 determined to be K_d = 1.3 ± 0.4 μM (K_d = 7.9 ± 1.1 μM for immobilized C-terminal a-Syn
509 peptide), which is significantly tighter than the binding affinity estimated by fitting the observed
510 NMR CSPs with a 1:1 single-site binding model (K_d = 169 ± 67 μM), which does not account for

511 the multivalent interaction involving the S1 and S2 motifs. We also measured the binding
512 affinities of the S1, S2, and Hsp90 peptides for immobilized hTPR2A. In agreement with the
513 results of the NMR competition experiments, the binding affinity of S2 (K_d = 32 ± 0.8 μM) is
514 higher than that of S1 (K_d = 87 ± 7.8 μM), while the K_d of the Hsp90 pentapeptide for hTPR2A
515 was 9.2 ± 0.7 μM (Figure S4), which agrees with a previous report ($K_d \approx$ 11 μM) [70]. Together,
516 these results demonstrate that the dynamic interaction between S1 and S2 of a-Syn and hTPR2A
517 significantly enhance the binding affinity in comparison to S1 and S2 separately.

518

519 **HOP inhibits a-Syn fibril formation**

520 Our previous work has demonstrated that alteration of STIP1 expression in mouse models
521 of α-synucleinopathy modulates the levels of insoluble pS129 a-Syn [36], suggesting that STIP1
522 may change the aggregation of a-Syn. Here, we further investigate if the direct interaction
523 between STIP1 and a-Syn changes a-Syn aggregation *in vitro*. To this end, we conducted
524 Thioflavin T (ThT) fluorescence assays to monitor a-Syn fibril formation. In the absence of
525 STIP1, ThT fluorescence increases after an initial lag phase (Fig. 3A) as amyloid fibrils of a-Syn
526 nucleate and begin to elongate as shown before [72–74]. Addition of STIP1 reduced ThT
527 fluorescence in a concentration dependent manner, with sub-stoichiometric concentrations of
528 STIP1 sufficient to significantly reduce ThT fluorescence (Fig. 3A). Notably, the addition of
529 mTPR2A reduced the ThT fluorescence of a-Syn to the same extent as full-length STIP1 at
530 equimolar concentrations, indicating that the mTPR2A domain alone is sufficient to attenuate a-
531 Syn fibrilization (Fig. 3A). To exclude the possibility that the changes in ThT fluorescence are
532 caused by non-specific crowding effects, we aggregated a-Syn in the presence of BSA at an
533 equal mg/ml ratio as mTPR2A at a 1:1 a-Syn to mTPR2A concentration, which resulted in only

534 minimal reduction of ThT fluorescence (Figure S5). Furthermore, we measured a-Syn fibril
535 formation in the presence of the TPR1 domain of STIP1 (mTPR1, which has only minimal
536 interactions with a-Syn [36]). NMR analysis of ^{15}N-labeled a-Syn in the presence of mTPR1
537 shows only minor peak shifts, indicating that mTPR1 interacts with a-Syn at very low affinity,
538 likely in a non-specific manner (Figure S6). The addition of mTPR1 reduced ThT fluorescence
539 to a much lesser extent compared to mTPR2A at similar stoichiometric ratios, confirming that
540 the effects observed for mTPR2A are not due to non-specific binding or crowding effects (Figs.
541 3B and 3C). Similarly, the addition of sub-stoichiometric concentrations of hTPR2A also
542 reduced the final steady-state of a-Syn ThT fluorescence in a concentration dependent manner
543 (Figs. 3D and 3E). Furthermore, both mTPR2A and hTPR2A substantially extended the lag
544 phase of a-Syn fibril formation (Fig. 3F). In addition, when we separated a-Syn aggregates into
545 soluble and insoluble fractions by centrifugation, the proportion of soluble a-Syn increases in the
546 presence of hTPR2A (Figure S7). Taken together, these results suggest that the direct interaction
547 between the TPR2A domain of STIP1/HOP and the C-terminal domain of a-Syn stabilizes a-Syn
548 in conformations that favour more soluble, non-fibrillar species.

549 We next asked if hTPR2A binding to a single site in the C-terminus of a-Syn, i.e., either
550 S1 or S2, is sufficient to alter fibril formation of a-Syn. We added hTPR2A to aggregation
551 reactions containing a-Syn bearing alanine substitutions at D119 and D121 (ΔS1) or at D135,
552 E137, and E139 (ΔS2). The addition of hTPR2A significantly reduced the ThT fluorescence of
553 both ΔS1 or ΔS2 a-Syn (Figure S8), demonstrating that hTPR2A can attenuate a-Syn fibril
554 formation by interacting independently with either the S1 or S2 motif within the C-terminus of a-
555 Syn.

556

557 **hTPR2A promotes the accumulation of amorphous a-Syn aggregates**

558 Since the overexpression of STIP1 in synucleinopathy mouse models increases the level
559 of insoluble phosphorylated a-Syn [36], we speculated that a-Syn initially accumulates in ThT-
560 negative forms in the presence of hTPR2A before eventually converting into fibrils. To test this,
561 we analyzed a-Syn incubated with hTPR2A by Electron Microscopy (EM). Note that the samples
562 contained a significantly higher concentration of a-Syn (175 μM) compared to our ThT
563 experiments to allow efficient fibril visualization. The fibrils observed after a-Syn was
564 aggregated alone for 5 days (Avg: 339 nm, Median: 272 nm) or in the presence of equimolar
565 mTPR1 as a non-specific binding control (Avg: 269 nm, Median: 231 nm) are longer than those
566 formed in the presence of hTPR2A (Avg: 246 nm, Median: 203 nm) (Fig. 3G). Furthermore, in
567 the presence of hTPR2A, amorphous protein inclusions averaging ~59 nm in diameter were
568 observed, often in close proximity to fibrils (Fig. 3G, white arrows), which were not observed
569 with a-Syn alone or treated with mTPR1. Notably, hTPR2A did not form these amorphous
570 aggregates in the absence of a-Syn (Figure S9). Our observations suggest that the addition of
571 hTPR2A attenuates fibril elongation by promoting either the formation or stabilization of
572 amorphous high molecular weight a-Syn species.

573

574 **hTPR2A Modulates the Early Stages of a-Syn Aggregation**

575 We next asked which stage of a-Syn fibril formation is affected by hTPR2A, specifically
576 whether it inhibits nucleation, stalls elongation, or disassembles existing fibrils. We added
577 equimolar hTPR2A to a-Syn fibrilization reactions prior to initiation of aggregation (0h), during
578 late lag phase (6h), elongation phase (12h & 24h), and steady-state phase (48h). The addition of

579 hTPR2A during late lag phase minimally extended the lag phase and reduced the ThT
580 fluorescence during elongation, but did not alter steady-state ThT fluorescence after prolonged
581 elongation (Figs. 4A-C). By contrast, hTPR2A added during the elongation phase or steady-state
582 phase did not alter ThT fluorescence (Figs. 4A-C). By far the strongest reduction effects on a-
583 Syn fibrilization occurred when hTPR2A was added prior to initiation, i.e., during the earliest
584 phases of a-Syn aggregation.

585 To further test if hTPR2A inhibits a-Syn fibril elongation in seeded aggregation assays,
586 we introduced additional a-Syn, either with or without hTPR2A, to aggregation reactions after
587 the ThT fluorescence reached steady-state. The addition of a-Syn increased the ThT fluorescence
588 beyond its previous steady-state value even in the presence of hTPR2A, indicating that hTPR2A
589 did not prevent incorporation of a-Syn into existing fibrils (Figure S10), supporting the notion
590 that hTPR2A influences a-Syn aggregation early, prior to fibril formation. Furthermore, hTPR2A
591 is unable to disassemble fibrils, such as the disaggregase Hsp104 [75], as its addition at steady-
592 state, i.e., after fibril formation, did not reduce ThT fluorescence.

593 Next, we investigated if addition of hTPR2A also inhibits fibril formation of a-Syn
594 variants such as pS129 and A53T a-Syn. The addition of equimolar concentrations of hTPR2A to
595 pS129 a-Syn aggregation reactions extended the lag phase and reduces the final steady-state
596 value of ThT fluorescence (Fig. 4D). We obtained similar results with the PD-associated A53T
597 mutant (Fig. 4E). Also, we found that the phosphorylation of A53T a-Syn at S129 did not
598 prevent hTPR2A from reducing the fibrilization of a-Syn (Fig. 4F).

599

600 **Binding of the Hsp90 pentapeptide to hTPR2A inhibits its ability to modulate a-Syn**
601 **aggregation**

602 We next investigated whether blocking the interaction between hTPR2A and a-Syn abolishes the
603 influence of hTPR2A on a-Syn aggregation. Since the Hsp90 pentapeptide (MEEVD) and the C-
604 terminal a-Syn peptide can effectively compete with the full-length a-Syn for hTPR2A binding,
605 we measured a-Syn fibril formation in the presence of equimolar hTPR2A and excess peptides
606 (10-fold molar ratio). The addition of excess C-terminal or pS129 C-terminal a-Syn peptides to
607 mixtures of a-Syn and hTPR2A shortened the lag phase of fibril formation by 45.9% (p =
608 0.0006) and 41.4% (p = 0.0012) respectively but did not prevent hTPR2A from reducing the
609 steady-state ThT fluorescence of a-Syn (Fig. 4G). On the other hand, the addition of excess
610 Hsp90 pentapeptide shortened the lag phase by 59.6% (p = 0.0004) and produced a similar
611 maximum ThT fluorescence as a-Syn alone, suggesting that excess Hsp90 can mitigate hTPR2A
612 regulation of a-Syn fibrilization (Fig. 4G). It is noteworthy that NMR ^{1}H-^{15}N HSQC analysis of
613 ^{15}N-labeled a-Syn in the presence of excess Hsp90 pentapeptide indicates that there are no direct
614 interactions between the peptide and a-Syn (Figure S11). Taken together, these results suggest
615 that blocking the binding of both S1 and S2 in the C-terminus of a-Syn to hTPR2A eradicates its
616 inhibition of a-Syn aggregation.

617

618 **hTPR2A induces the formation of amorphous high molecular weight a-Syn species**

619 Our results suggest that the interaction between hTPR2A and the C-terminal domain of a-
620 Syn influences the pre-fibrillar stages of a-Syn aggregation. We next employed Atomic Force
621 Microscopy (AFM) to further characterize the morphology of pre-fibrillar a-Syn species. We

622 visualized samples taken at different time points from aggregation reactions containing 175 μM
623 a-Syn in the absence or presence of equimolar mTPR1 or hTPR2A by AFM. The a-Syn fibrils
624 formed in the presence of hTPR2A are shorter in length compared to reaction carried out in the
625 presence of mTPR1 or a-Syn alone (Figure S12A). Moreover, fibril load (measured as the
626 percentage of the surface area occupied by fibrils) of a-Syn samples aggregated in the presence
627 of hTPR2A are significantly reduced compared to a-Syn aggregated alone or in the presence of
628 mTPR1 (Figure S12B). Furthermore, we observed amorphous, high molecular-weight a-Syn
629 species in samples aggregated in the presence of hTPR2A (Figure S12A). We performed
630 aggregation reactions with reduced a-Syn concentrations to decrease the rate of fibril formation,
631 allowing the capture and analysis of oligomeric species. The a-Syn oligomers visualized by AFM
632 were transient, appeared after 2-3 days and disappeared upon fibril nucleation (day 3-4).
633 However, in the presence of hTPR2A, many amorphous species were present after 1 day of
634 aggregation and can be observed at all subsequent time points (Fig. 5A). The amorphous a-Syn
635 species formed in the presence of hTPR2A are of a broad size range and are significantly larger
636 than the oligomers measured in a-Syn samples aggregated alone or in the presence of mTPR1, as
637 observed on the 3rd day of aggregation (Figs. 5B and 5C). While oligomers of a-Syn were small
638 and transient, the amorphous a-Syn species formed in the presence of hTPR2A persisted for
639 several days and increased in size, as is apparent by correlation plots and distributions of their
640 diameter and height (Figure S12C).

641 To verify the aggregate size differences, we monitored a-Syn species present in
642 aggregated samples by Dynamic Light Scattering (DLS). Aligning with EM and AFM results,
643 DLS analysis showed a significant reduction in the size of the fibrils formed in the presence of
644 hTPR2A. Also, in agreement with AFM, the size of the oligomers formed in the absence of

645 hTPR2A are significantly smaller than the pre-fibrillar a-Syn species formed in the presence of
646 hTPR2A (Figs. 5D and 5E). Taken together, our results suggest that, in contrast to the oligomers
647 formed by a-Syn alone, the interaction between hTPR2A and the C-terminal domain of a-Syn
648 promotes the formation of larger amorphous a-Syn species that do not efficiently transition into
649 fibrils. These accumulating amorphous a-Syn species formed in the presence of hTPR2A are not
650 static and continue to increase in size as aggregation progresses (Fig. 5A and Figure S12A),
651 suggesting that hTPR2A may stabilize soluble a-Syn aggregates thereby facilitating their
652 continued growth rather than transition to fibrils.

653

654 **hTPR2A associates with high molecular weight species of a-Syn during aggregation**

655 Molecular chaperones that interact with the N-terminal domain of a-Syn, such as Hsp90
656 and Hsp70, maintain their N-terminal interactions with oligomeric a-Syn [26]. To test if hTPR2A
657 remains bound to the C-terminal domain of a-Syn within the amorphous high-molecular weight
658 a-Syn species, we analyzed aggregated samples using size-exclusion chromatography. Samples
659 of hTPR2A that were incubated at 37 ºC for 24 hours in a shaking incubator before injecting
660 onto a Superdex 200 10/300 size exclusion column elute as a sharp peak corresponding to
661 monomeric hTPR2A (Fig. 5F). On the other hand, when hTPR2A is incubated with equimolar a-
662 Syn, hTPR2A elutes in fractions corresponding to monomeric hTPR2A and co-elutes with a-Syn
663 in fractions corresponding to monomeric and high molecular weight species of a-Syn (Figs. 5F
664 and 5G). The co-elution of hTPR2A and a-Syn in high molecular weight fractions suggests that
665 hTPR2A interacts with both monomeric a-Syn and a-Syn within the amorphous high molecular
666 weight species.

667

668 **Co-expression of HOP and a-Syn in yeast alters a-Syn localization and increases a-Syn**
669 **toxicity**

670 To test if the interaction between a-Syn and HOP modifies a-Syn aggregation and
671 toxicity within a cellular context, we employed a well-established yeast model of a-Syn toxicity
672 [76,77]. Low-copy expression of a-Syn in yeast does not impart a growth defect at optimal
673 growth conditions (30 ºC) but reduces growth under heat stress conditions (37 ºC) [76,78]. Co-
674 expression of HOP and a-Syn unmasks a growth defect in yeast even in the absence of heat stress
675 (Fig. 6A) and exacerbates the growth defect under heat stress conditions (Fig. 6B). Treatment
676 with Hsp90 ATPase inhibitor Radicicol did not recover the growth phenotype observed with co-
677 expression of HOP and a-Syn at either optimal (Fig. 6C) or heat stress temperatures (Fig. 6D),
678 suggesting that the growth defect is due to the interaction between HOP and a-Syn, independent
679 of Hsp90 ATP-hydrolysis.

680 To test if expression of HOP alters the localization of a-Syn *in vivo*, we monitored yeast
681 cells expressing HOP and a-Syn-YFP from low copy number plasmids by fluorescent
682 microscopy. In agreement with previous studies [76], we observed a-Syn-YFP localization at the
683 plasma membrane and in concentrated cytoplasmic inclusions, which increase in number during
684 heat stress (37 ºC). Co-expressing HOP with a-Syn-YFP did not change the proportion of cells
685 containing cytoplasmic a-Syn-YFP inclusions when grown under optimal conditions. However,
686 it significantly reduced this proportion under heat stress conditions (Fig. 6E). To test whether the
687 change in a-Syn localization is caused by the interaction between HOP and a-Syn or a passing of
688 a-Syn to Hsp90, cells were treated with Radicicol at concentrations below the threshold to induce
689 the heat shock response [79]. Treatment with Radicicol did not alter the effect of HOP co-

690 expression in reducing the proportion of cells with cytoplasmic inclusions after heat stress (Fig.
691 6E), suggesting that HOP changes a-Syn-YFP localization independently of Hsp90 ATPase
692 activity.

693

694 **Amorphous high molecular weight a-Syn species formed in the presence of hTPR2A**
695 **contain cytotoxic a-Syn oligomers**

696 Since HOP altered the toxicity of a-Syn when co-expressed in the yeast model system,
697 we tested if the amorphous high molecular weight a-Syn species formed in the presence of
698 hTPR2A resemble cytotoxic a-Syn observed in synucleinopathy models [80,81]. The oligomer
699 content of samples from aggregation mixtures containing a-Syn with or without the addition of
700 hTPR2A were quantified using immunodetection by the A11 antibody, which specifically
701 recognizes pre-fibrillar a-Syn assemblies, including pathogenic a-Syn oligomers [80,81]. We
702 applied a-Syn species formed at different time points upon incubation with hTPR2A to a
703 membrane and probed with the A11 antibody. Significantly more A11-positive signal was
704 detected in samples of a-Syn aggregated in the presence of hTPR2A across all time points
705 measured as compared to reaction performed in its absence (Fig. 6F). These results suggest that
706 the amorphous high molecular weight a-Syn species that accumulate in the presence of hTPR2A
707 are comprised of or resemble the oligomeric a-Syn species that have been observed in
708 synucleinopathy models [81,82]. Furthermore, the increased A11 signal confirms that a-Syn
709 aggregated in the presence of hTPR2A forms increased levels of pre-fibrillar a-Syn species.

710

711 **hTPR2A exacerbates the toxicity of aggregated a-Syn on SH-SY5Y cells**

712 Since smaller pre-fibrillar species are more toxic to neuronal cells than larger fibrillar a-
713 Syn [83], we tested if a-Syn samples aggregated in the presence of hTPR2A are cytotoxic to cells
714 by assessing the viability of SH-SY5Y human neuroblastoma cells treated with different
715 aggregated samples of a-Syn. When cells were treated with samples from aggregation mixtures
716 containing only a-Syn (35 μM initial monomer concentration), no reduction on cell viability was
717 observed for any of the aggregation times tested. By contrast, treatment with samples from
718 aggregation mixtures containing a-Syn and equimolar hTPR2A from all timepoints tested caused
719 a significant reduction in cell viability as compared to cells topically treated with aggregated a-
720 Syn alone (Fig. 6G). These results show that the accumulation of amorphous high molecular
721 weight a-Syn species caused by hTPR2A binding increases sample toxicity relative to mostly
722 fibrillar a-Syn aggregates.

723 ## Discussion

724 Our study deciphers how the molecular co-chaperone STIP1/HOP prevents the
725 fibrilization of a-Syn by steering it toward the formation of highly toxic oligomeric species. The
726 two independent low-affinity binding motifs in the C-terminus of a-Syn compete for a single
727 interface on the TPR2A domain of STIP1/HOP. This dynamic binding facilitates transient
728 interactions between these two proteins and dictates the specificity for the TPR2A over the other
729 TPR domains of STIP1/HOP.

730 Molecular chaperones and co-chaperones help maintain protein functions during
731 misfolding stress [84]. Of note, however, they can also stabilize or perpetuate toxic
732 conformations of misfolded proteins [24,25,85–87]. Our previous studies in mouse models found
733 that STIP1 interacts with a-Syn and that decreased levels of STIP1 mitigate a-Syn toxicity and
734 reduce the levels of S129 phosphorylated a-Syn, a neuropathological marker of
735 synucleinopathies. Conversely, increased STIP1 levels exacerbate synucleinopathy-associated
736 phenotypes and the accumulation of S129 phosphorylated a-syn [36]. Our biochemical analyses
737 presented here reveal how the interaction between a-Syn and STIP1/HOP promotes the
738 formation of oligomeric, non-fibrillar conformers of a-Syn. In addition, a-Syn retains its binding
739 to STIP1/HOP within these amorphous aggregates, further attenuating the transition into fibrils
740 and promoting the accumulation of amorphous oligomeric species. We have found previously
741 that the binding of STIP1 enhances the S129 phosphorylation of a-Syn. The retained binding of
742 STIP1/HOP to the amorphous aggregates of a-Syn may explain the accumulation of
743 phosphorylated S129 a-Syn aggregates in the synucleinopathy mouse model with increased
744 STIP1 levels [36].

745 We further show that STIP1/HOP does not require ATP-dependent chaperoning functions
746 or other contributions by Hsp90 and Hsp70 to promote the accumulation of oligomeric a-Syn.
747 Rather, STIP1/HOP modulates a-Syn aggregation through a holdase mechanism that only
748 requires a direct interaction [88,89]. There are specific scenarios that may favour a holdase
749 function of STIP1/HOP, such as in aged cells that are challenged by an ongoing proteostasis
750 crisis [90,91], where STIP1/HOP favours client proteins over Hsp90 and Hsp70 [92]. This
751 change in interaction preference may be a consequence of Hsp90 and Hsp70 being tied up in
752 interactions with misfolded proteins [44,92] and ATP depletion, thereby favouring the holdase
753 functions of STIP1/HOP [93–95]. In addition, both STIP1/HOP and a-Syn are found in
754 extracellular vesicles [47,96,97] which can explain why a-Syn phosphorylated at S129 is
755 enriched inside these vesicles [98]. When secreted into the ATP-deprived extracellular space, the
756 holdase function of STIP1/HOP may alter the interaction between misfolded a-Syn and
757 extracellular proteins, as observed between STIP1/HOP and PrP^{C} [99,100], thereby contributing
758 to cell-to-cell spreading of misfolded a-Syn. Moreover, a-Syn oligomers have been previously
759 shown to coopt PrP^{C}, mGluR5 and NMDA receptors to cause synaptic toxicity, suggesting
760 another mechanism by which interaction of STIP1 and a-Syn may act [35,101]. The holdase
761 activity of STIP1/HOP generally mitigates the toxicity associated with misfolded proteins during
762 proteostasis stress [43,44,102]. Yet, we demonstrate here for a-Syn that it can also have
763 detrimental effects on aggregation-prone proteins.

764 Many molecular chaperones, such as Hsp90 and Hsp70, reduce the toxicity of a-Syn
765 oligomers by binding a-Syn and masking regions of its N-terminal domain, thereby preventing
766 membrane disruption and cellular toxicity [6,26–28,30]. Intriguingly, our data suggest that
767 Hsp90 and a-Syn can compete for binding to STIP1/HOP, suggesting that the relative abundance

768 and localization of each of these molecular chaperones may determine a-Syn toxicity. Our
769 previous studies show that during protein misfolding stress, STIP1/HOP accumulates into
770 defined cytoplasmic areas along with soluble ubiquitinated proteins [44]. These areas may favour
771 the deleterious interaction between a-Syn and STIP1/HOP over the protective binding between a-
772 Syn and Hsp90.

773 The same key acidic residues in the C-terminal domain of a-Syn which interact with
774 STIP1/HOP also mediate binding to FABP3 [33], tau [103], and Ca^{2+} [104], all of which also
775 promote a-Syn oligomerization [31–33,36]. These acidic residues are essential for recruiting
776 monomeric and oligomeric a-Syn into existing fibrils [18], and alterations in the C-terminal
777 charge of a-Syn modulate the kinetics of fibril formation [7–10]. Specific residues in the N-
778 terminal domain of a-syn and the hydrophobic NAC region are key contact sites within a-Syn
779 fibrils [105–107], whereas the negatively charged C-terminal domain remains disordered,
780 forming a fuzzy coat around fibrils that facilitate the "seeding" process by recruiting a-Syn
781 monomers and oligomers through their positively charged N-terminus [18].

782 With all these features in mind, we propose a general mechanism by which proteins
783 interacting with the C-terminus of a-Syn masks its negative charge, thereby reducing the intra-
784 and inter-molecular N-C terminal interactions. Consequently, binding of STIP1/HOP, FABP3,
785 tau, and calcium ions to a-Syn may lower the kinetic barrier to form highly toxic oligomers and
786 simultaneously prevent the conversion of oligomers into fibrils (Fig. 7). Thus, N-terminal
787 interactions, such as those observed for Hsp90 and Hsp70, may prevent the accumulation of
788 cytotoxicity a-Syn oligomers, whereas C-terminal interactions, like STIP1/HOP, promote the
789 accumulation of cytotoxic a-Syn (Fig. 7). This baffling dichotomy deserves consideration in
790 studies seeking to determine the effect of molecular chaperones and other proteostatic pathways

791 on the toxicity of a-Syn in PD and LBD. Moreover, our findings may apply to other aggregation-
792 prone proteins associated with neurodegenerative diseases and indicate a possible protective role
793 of fibrillar, amyloid-like aggregates and detrimental effects of molecular chaperones that prevent
794 fibrillar aggregation and favour the accumulation of highly toxic oligomers.

795

796 Data, Materials, and Software Availability

797 All study data are included in the article and/or Supplemental Information.

798

799 Acknowledgments

800 We thank the Biomolecular NMR and BioCORE facilities (Western University) for their
801 assistance and use of equipment. Digital Research Alliance of Canada provided the
802 computational resources. Thank you to Karling Frankel for creating the digital design of our
803 aggregation model schematic.

804

805 Funding

806 W.Y.C is supported by a Discovery Grant (RGPIN-2019-06711) from the Natural Sciences and
807 Engineering Research Council (NSERC), M.D. is supported by a Discovery Grant (RGPIN-
808 2024-05867) from the NSERC, and M.K. thanks the NSERC and the Canada Research Chairs
809 Program. E.D.C.P. was financially supported by grant from the Canadian Institutes for Health
810 Research (CIHR FDN–154301 to E.A.F). E.A.F is holder of a Canada Research Chair (Tier 1) in

Parkinson Disease and the Canadian Consortium on Neurodegeneration in Aging (CCNA) Foundation. M.A.M.P. received support from the Canadian Institutes of Health Research (CIHR, PJT 162431, PJT 195987), NSERC (03592-2021 RGPIN), BrainsCAN Canada First Research Excellence Fund Accelerator Awards (Initiative for Translational Neuroscience), Canada Foundation for Innovation, Ontario Research Fund, Alzheimer's Association (USA), Weston Brain Institute, Weston Family Foundation, as well as support from New Frontiers Research Fund (NFRFT-2022-00051, TRIDENT). M.A.M.P. is a Tier I Canada Research Chair in Neurochemistry of Dementia.

Author Contributions

B.S.R., designed and performed research, analyzed data, generated figures, and wrote the paper. C.J.W. and J.L performed research, analyzed data, and aided in figure generation. R.M.L., J.C.J.C., and E.D.C.P. performed research and analyzed data. M.K., T.M.D., and E.A.F designed research and contributed analytical tools. M.A.M.P, J.L, M.L.D, and W.Y.C designed research, contributed reagents or analytical tools, and wrote the paper. All authors aided in revising the manuscript's intellectual content. All authors read and approved the submitted manuscript.

Competing interests

The authors declare no competing interests.

Ethics approval and consent to participate

832 N/A

833

834 ## Consent for publication

835 N/A

836

837 ## Abbreviations

838 **a-Syn:** alpha-synuclein

839 **LBD:** Lewy Body Dementia

840 **PD:** Parkinson's disease

841 **NAC:** non-Aβ component

842 **IDP:** intrinsically disordered protein

843 **FABP3:** fatty acid binding protein 3

844 **PrP^C:** cellular prion protein

845 **STIP1:** Stress inducible phosphoprotein 1

846 **HOP:** Hsp-organizing protein

847 **TPR:** tetratricopeptide repeat domain

848 **DP:** aspartate and proline rich domain

849 **TDP-43:** TAR DNA-binding protein 43

850 **pS129 a-Syn:** alpha-synuclein phosphorylated at serine 129

851 **mTPR2A:** mouse STIP1-TPR2A domain

852 **hTPR2A:** human HOP-TPR2A domain

853 **NMR:** Nuclear Magnetic Resonance

854 **HSQC:** Heteronuclear Single Quantum Coherence

855 **CSPs:** chemical shift perturbations

856 **S1:** residues 117-127 of alpha-synuclein

857 **S2:** residues 130-140 of alpha-synuclein

858 **MD:** molecular dynamics

859 **BLI:** Bio-Layer Interferometry

860 **ThT:** Thioflavin T

861 Δ**S1:** alpha-synuclein bearing alanine substitutions at D119 and D121

862 Δ**S2:** alpha-synuclein bearing alanine substitutions at D135, E137, and E139

863 **EM:** Electron Microscopy

864 **AFM:** Atomic Force Microscopy

865 **DLS:** Dynamic Light Scattering

866

867

868 **References**

869 1. Santos J, Pallarès I, Ventura S. Is a cure for Parkinson's disease hiding inside us? Trends
870 Biochem Sci. 2022;47:641–4.

871 2. Twohig D, Nielsen HM. α-synuclein in the pathophysiology of Alzheimer's disease. Mol
872 Neurodegener. 2019;14:23.

873 3. Dimant H, Ebrahimi-Fakhari D, McLean PJ. Molecular chaperones and co-chaperones in
874 Parkinson disease. Neuroscientist. 2012;18:589–601.

875 4. Burré J. The Synaptic Function of α-Synuclein. J Parkinsons Dis. 2015;5:699–713.

876 5. Shahmoradian SH, Lewis AJ, Genoud C, Hench J, Moors TE, Navarro PP, et al. Lewy
877 pathology in Parkinson's disease consists of crowded organelles and lipid membranes. Nat
878 Neurosci. 2019;22:1099–109.

879 6. Fusco G, Chen SW, Williamson PTF, Cascella R, Perni M, Jarvis JA, et al. Structural basis
880 of membrane disruption and cellular toxicity by α-synuclein oligomers. Science.
881 2017;358:1440–3.

882 7. Buell AK, Galvagnion C, Gaspar R, Sparr E, Vendruscolo M, Knowles TPJ, et al. Solution
883 conditions determine the relative importance of nucleation and growth processes in α-
884 synuclein aggregation. Proc Natl Acad Sci U S A. 2014;111:7671–6.

885 8. Levitan K, Chereau D, Cohen SIA, Knowles TPJ, Dobson CM, Fink AL, et al. Conserved C-
886 terminal charge exerts a profound influence on the aggregation rate of α-synuclein. J Mol
887 Biol. 2011;411:329–33.

888 9. Hoyer W, Cherny D, Subramaniam V, Jovin TM. Impact of the acidic C-terminal region
889 comprising amino acids 109-140 on alpha-synuclein aggregation in vitro. Biochemistry.
890 2004;43:16233–42.

891 10. Murray IVJ, Giasson BI, Quinn SM, Koppaka V, Axelsen PH, Ischiropoulos H, et al. Role of
892 alpha-synuclein carboxy-terminus on fibril formation in vitro. Biochemistry. 2003;42:8530–
893 40.

894 11. Lesage S, Anheim M, Letournel F, Bousset L, Honoré A, Rozas N, et al. G51D α-
895 synuclein mutation causes a novel parkinsonian-pyramidal syndrome. Ann Neurol.
896 2013;73:459–71.

897 12. Proukakis C, Dudzik CG, Brier T, MacKay DS, Cooper JM, Millhauser GL, et al. A novel α-
898 synuclein missense mutation in Parkinson disease. Neurology. 2013;80:1062–4.

13. Hoffman-Zacharska D, Koziorowski D, Ross OA, Milewski M, Poznanski JA, Jurek M, et al. Novel A18T and pA29S substitutions in α-synuclein may be associated with sporadic Parkinson's disease. Parkinsonism Relat Disord. 2013;19:1057–60.

14. Zarranz JJ, Alegre J, Gómez-Esteban JC, Lezcano E, Ros R, Ampuero I, et al. The new mutation, E46K, of alpha-synuclein causes Parkinson and Lewy body dementia. Ann Neurol. 2004;55:164–73.

15. Forno LS. Neuropathology of Parkinson's disease. J Neuropathol Exp Neurol. 1996;55:259–72.

16. Kumar ST, Mahul-Mellier A-L, Hegde RN, Rivière G, Moons R, Ibáñez de Opakua A, et al. A NAC domain mutation (E83Q) unlocks the pathogenicity of human alpha-synuclein and recapitulates its pathological diversity. Sci Adv. 2022;8:eabn0044.

17. Janowska MK, Wu K-P, Baum J. Unveiling transient protein-protein interactions that modulate inhibition of alpha-synuclein aggregation by beta-synuclein, a pre-synaptic protein that co-localizes with alpha-synuclein. Sci Rep. 2015;5:15164.

18. Khare SD, Chinchilla P, Baum J. Multifaceted interactions mediated by intrinsically disordered regions play key roles in alpha synuclein aggregation. Curr Opin Struct Biol. 2023;80:102579.

19. Williams JK, Yang X, Atieh TB, Olson MP, Khare SD, Baum J. Multi-Pronged Interactions Underlie Inhibition of α-Synuclein Aggregation by β-Synuclein. J Mol Biol. 2018;430:2360–71.

20. Han D, Zheng W, Wang X, Chen Z. Proteostasis of α-Synuclein and Its Role in the Pathogenesis of Parkinson's Disease. Front Cell Neurosci. 2020;14:45.

21. Manecka D-L, Vanderperre B, Fon EA, Durcan TM. The Neuroprotective Role of Protein Quality Control in Halting the Development of Alpha-Synuclein Pathology. Front Mol Neurosci. 2017;10:311.

22. De Mattos EP, Wentink A, Nussbaum-Krammer C, Hansen C, Bergink S, Melki R, et al. Protein Quality Control Pathways at the Crossroad of Synucleinopathies. J Parkinsons Dis. 2020;10:369–82.

23. Burmann BM, Gerez JA, Matečko-Burmann I, Campioni S, Kumari P, Ghosh D, et al. Regulation of α-synuclein by chaperones in mammalian cells. Nature. 2020;577:127–32.

24. Rutledge BS, Choy W-Y, Duennwald ML. Folding or holding?-Hsp70 and Hsp90 chaperoning of misfolded proteins in neurodegenerative disease. J Biol Chem. 2022;298:101905.

932 25. Falsone SF, Kungl AJ, Rek A, Cappai R, Zangger K. The molecular chaperone Hsp90
933 modulates intermediate steps of amyloid assembly of the Parkinson-related protein alpha-
934 synuclein. J Biol Chem. 2009;284:31190–9.

935 26. Daturpalli S, Waudby CA, Meehan S, Jackson SE. Hsp90 inhibits α-synuclein
936 aggregation by interacting with soluble oligomers. J Mol Biol. 2013;425:4614–28.

937 27. Luk KC, Mills IP, Trojanowski JQ, Lee VM-Y. Interactions between Hsp70 and the
938 hydrophobic core of alpha-synuclein inhibit fibril assembly. Biochemistry. 2008;47:12614–
939 25.

940 28. Tao J, Berthet A, Citron YR, Tsiolaki PL, Stanley R, Gestwicki JE, et al. Hsp70 chaperone
941 blocks α-synuclein oligomer formation via a novel engagement mechanism. J Biol Chem.
942 2021;296:100613.

943 29. Huang C, Cheng H, Hao S, Zhou H, Zhang X, Gao J, et al. Heat shock protein 70 inhibits
944 alpha-synuclein fibril formation via interactions with diverse intermediates. J Mol Biol.
945 2006;364:323–36.

946 30. Chaari A, Eliezer D, Ladjimi M. The C-terminal α-helices of mammalian Hsc70 play a
947 critical role in the stabilization of α-synuclein binding and inhibition of aggregation. Int J Biol
948 Macromol. 2016;83:433–41.

949 31. Nielsen MS, Vorum H, Lindersson E, Jensen PH. Ca2+ binding to alpha-synuclein
950 regulates ligand binding and oligomerization. J Biol Chem. 2001;276:22680–4.

951 32. Vasili E, Dominguez-Meijide A, Outeiro TF. Spreading of α-Synuclein and Tau: A
952 Systematic Comparison of the Mechanisms Involved. Front Mol Neurosci. 2019;12:107.

953 33. Fukui N, Yamamoto H, Miyabe M, Aoyama Y, Hongo K, Mizobata T, et al. An α-synuclein
954 decoy peptide prevents cytotoxic α-synuclein aggregation caused by fatty acid binding
955 protein 3. J Biol Chem. 2021;296:100663.

956 34. Agarwal A, Arora L, Rai SK, Avni A, Mukhopadhyay S. Spatiotemporal modulations in
957 heterotypic condensates of prion and α-synuclein control phase transitions and amyloid
958 conversion. Nat Commun. 2022;13:1154.

959 35. Vieira TCRG, Barros CA, Domingues R, Outeiro TF. PrP meets alpha-synuclein:
960 Molecular mechanisms and implications for disease. J Neurochem. 2024;168:1625–39.

961 36. Lackie RE, de Miranda AS, Lim MP, Novikov V, Madrer N, Karunatilleke NC, et al. Stress-
962 inducible phosphoprotein 1 (HOP/STI1/STIP1) regulates the accumulation and toxicity of α-
963 synuclein in vivo. Acta Neuropathol. 2022;144:881–910.

964 37. Rösener NS, Gremer L, Wördehoff MM, Kupreichyk T, Etzkorn M, Neudecker P, et al.
965 Clustering of human prion protein and α-synuclein oligomers requires the prion protein N-
966 terminus. Commun Biol. 2020;3:365.

967 38. Bhattacharya K, Picard D. The Hsp70-Hsp90 go-between Hop/Stip1/Sti1 is a
968 proteostatic switch and may be a drug target in cancer and neurodegeneration. Cell Mol
969 Life Sci. 2021;78:7257–73.

970 39. Southworth DR, Agard DA. Client-loading conformation of the Hsp90 molecular
971 chaperone revealed in the cryo-EM structure of the human Hsp90:Hop complex. Mol Cell.
972 2011;42:771–81.

973 40. Wang RY-R, Noddings CM, Kirschke E, Myasnikov AG, Johnson JL, Agard DA. Structure of
974 Hsp90-Hsp70-Hop-GR reveals the Hsp90 client-loading mechanism. Nature.
975 2022;601:460–4.

976 41. Brinker A, Scheufler C, Von Der Mulbe F, Fleckenstein B, Herrmann C, Jung G, et al.
977 Ligand discrimination by TPR domains. Relevance and selectivity of EEVD-recognition in
978 Hsp70 x Hop x Hsp90 complexes. J Biol Chem. 2002;277:19265–75.

979 42. Carrigan PE, Nelson GM, Roberts PJ, Stoffer J, Riggs DL, Smith DF. Multiple domains of
980 the co-chaperone Hop are important for Hsp70 binding. J Biol Chem. 2004;279:16185–93.

981 43. Bhattacharya K, Weidenauer L, Luengo TM, Pieters EC, Echeverría PC, Bernasconi L, et
982 al. The Hsp70-Hsp90 co-chaperone Hop/Stip1 shifts the proteostatic balance from folding
983 towards degradation. Nat Commun. 2020;11:5975.

984 44. Rutledge BS, Kim YJ, McDonald DW, Jurado-Coronel JC, Prado MAM, Johnson JL, et al.
985 Stress-inducible phosphoprotein 1 (Sti1/Stip1/Hop) sequesters misfolded proteins during
986 stress. FEBS J. 2024;

987 45. Beckley SJ, Hunter MC, Kituyi SN, Wingate I, Chakraborty A, Schwarz K, et al.
988 STIP1/HOP Regulates the Actin Cytoskeleton through Interactions with Actin and Changes
989 in Actin-Binding Proteins Cofilin and Profilin. Int J Mol Sci. 2020;21:3152.

990 46. Tsai C-L, Chao A-S, Jung S-M, Lin C-Y, Chao A, Wang T-H. Stress-induced
991 phosphoprotein 1 acts as a scaffold protein for glycogen synthase kinase-3 beta-mediated
992 phosphorylation of lysine-specific demethylase 1. Oncogenesis. 2018;7:31.

993 47. Hajj GNM, Arantes CP, Dias MVS, Roffé M, Costa-Silva B, Lopes MH, et al. The
994 unconventional secretion of stress-inducible protein 1 by a heterogeneous population of
995 extracellular vesicles. Cell Mol Life Sci. 2013;70:3211–27.

996 48. Fonseca ACC da, Romão L, Amaral RF, Assad Kahn S, Lobo D, Martins S, et al.
997 Microglial stress inducible protein 1 promotes proliferation and migration in human
998 glioblastoma cells. Neuroscience. 2012;200:130–41.

999 49. Tsai C-L, Tsai C-N, Lin C-Y, Chen H-W, Lee Y-S, Chao A, et al. Secreted stress-induced
1000 phosphoprotein 1 activates the ALK2-SMAD signaling pathways and promotes cell
1001 proliferation of ovarian cancer cells. Cell Rep. 2012;2:283–93.

1002 50. Lin LT-W, Razzaq A, Di Gregorio SE, Hong S, Charles B, Lopes MH, et al. Hsp90 and its
1003 co-chaperone Sti1 control TDP-43 misfolding and toxicity. FASEB J. 2021;35:e21594.

1004 51. Beraldo FH, Soares IN, Goncalves DF, Fan J, Thomas AA, Santos TG, et al. Stress-
1005 inducible phosphoprotein 1 has unique cochaperone activity during development and
1006 regulates cellular response to ischemia via the prion protein. The FASEB Journal.
1007 2013;27:3594–607.

1008 52. Lackie RE, Marques-Lopes J, Ostapchenko VG, Good S, Choy W-Y, van Oosten-Hawle P,
1009 et al. Increased levels of Stress-inducible phosphoprotein-1 accelerates amyloid-β
1010 deposition in a mouse model of Alzheimer's disease. Acta Neuropathol Commun.
1011 2020;8:143.

1012 53. Maciejewski A, Ostapchenko VG, Beraldo FH, Prado VF, Prado MAM, Choy W-Y.
1013 Domains of STIP1 responsible for regulating PrPC-dependent amyloid-β oligomer toxicity.
1014 Biochem J. 2016;473:2119–30.

1015 54. Delaglio F, Grzesiek S, Vuister GW, Zhu G, Pfeifer J, Bax A. NMRPipe: a multidimensional
1016 spectral processing system based on UNIX pipes. J Biomol NMR. 1995;6:277–93.

1017 55. Johnson BA. From Raw Data to Protein Backbone Chemical Shifts Using NMRFx
1018 Processing and NMRViewJ Analysis. Methods Mol Biol. 2018;1688:257–310.

1019 56. Williamson MP. Using chemical shift perturbation to characterise ligand binding. Prog
1020 Nucl Magn Reson Spectrosc. 2013;73:1–16.

1021 57. Jorgensen WL, Chandrasekhar J, Madura JD, Impey RW, Klein ML. Comparison of simple
1022 potential functions for simulating liquid water. Journal of Chemical Physics. 1983;79:926–
1023 35.

1024 58. Huang J, Rauscher S, Nawrocki G, Ran T, Feig M, de Groot BL, et al. CHARMM36m: an
1025 improved force field for folded and intrinsically disordered proteins. Nat Methods.
1026 2017;14:71–3.

1027 59. Piana S, Donchev AG, Robustelli P, Shaw DE. Water dispersion interactions strongly
1028 influence simulated structural properties of disordered protein states. J Phys Chem B.
1029 2015;119:5113–23.

1030 60. Abraham MJ, Murtola T, Schulz R, Páll S, Smith JC, Hess B, et al. GROMACS: High
1031 performance molecular simulations through multi-level parallelism from laptops to
1032 supercomputers. SoftwareX. 2015;1–2:19–25.

1033 61. Bussi G, Donadio D, Parrinello M. Canonical sampling through velocity rescaling. J
1034 Chem Phys. 2007;126:014101.

1035 62. Parrinello M, Rahman A. Polymorphic transitions in single crystals: A new molecular
1036 dynamics method. Journal of Applied Physics. 1981;52:7182–90.

1037 63. Darden T, York D, Pedersen L. Particle mesh Ewald: An N·log(N) method for Ewald sums
1038 in large systems. The Journal of Chemical Physics. 1993;98:10089–92.

1039 64. Hess B. P-LINCS: A Parallel Linear Constraint Solver for Molecular Simulation. J Chem
1040 Theory Comput. 2008;4:116–22.

1041 65. Burke KA, Godbey J, Legleiter J. Assessing mutant huntingtin fragment and
1042 polyglutamine aggregation by atomic force microscopy. Methods. 2011;53:275–84.

1043 66. Kawai S, Hashimoto W, Murata K. Transformation of Saccharomyces cerevisiae and
1044 other fungi: methods and possible underlying mechanism. Bioeng Bugs. 2010;1:395–403.

1045 67. Petropavlovskiy AA, Tauro MG, Lajoie P, Duennwald ML. A Quantitative Imaging-Based
1046 Protocol for Yeast Growth and Survival on Agar Plates. STAR Protoc. 2020;1:100182.

1047 68. Petroi D, Popova B, Taheri-Talesh N, Irniger S, Shahpasandzadeh H, Zweckstetter M, et
1048 al. Aggregate clearance of α-synuclein in Saccharomyces cerevisiae depends more on
1049 autophagosome and vacuole function than on the proteasome. J Biol Chem.
1050 2012;287:27567–79.

1051 69. Wu K-P, Kim S, Fela DA, Baum J. Characterization of conformational and dynamic
1052 properties of natively unfolded human and mouse alpha-synuclein ensembles by NMR:
1053 implication for aggregation. J Mol Biol. 2008;378:1104–15.

1054 70. Scheufler C, Brinker A, Bourenkov G, Pegoraro S, Moroder L, Bartunik H, et al. Structure
1055 of TPR domain-peptide complexes: critical elements in the assembly of the Hsp70-Hsp90
1056 multichaperone machine. Cell. 2000;101:199–210.

1057 71. Deng Y, Efremov AK, Yan J. Modulating binding affinity, specificity, and configurations by
1058 multivalent interactions. Biophys J. 2022;121:1868–80.

1059 72. Sulatskaya AI, Rodina NP, Sulatsky MI, Povarova OI, Antifeeva IA, Kuznetsova IM, et al.
1060 Investigation of α-Synuclein Amyloid Fibrils Using the Fluorescent Probe Thioflavin T. Int J
1061 Mol Sci. 2018;19:2486.

1062 73. Xue C, Lin TY, Chang D, Guo Z. Thioflavin T as an amyloid dye: fibril quantification,
1063 optimal concentration and effect on aggregation. R Soc Open Sci. 2017;4:160696.

1064 74. Wördehoff MM, Hoyer W. α-Synuclein Aggregation Monitored by Thioflavin T
1065 Fluorescence Assay. Bio Protoc. 2018;8:e2941.

1066 75. Mack KL, Kim H, Barbieri EM, Lin J, Braganza S, Jackrel ME, et al. Tuning Hsp104
1067 specificity to selectively detoxify α-synuclein. Mol Cell. 2023;83:3314-3332.e9.

1068 76. Outeiro TF, Lindquist S. Yeast cells provide insight into alpha-synuclein biology and
1069 pathobiology. Science. 2003;302:1772–5.

1070 77. Sancenon V, Lee S-A, Patrick C, Griffith J, Paulino A, Outeiro TF, et al. Suppression of α-
1071 synuclein toxicity and vesicle trafficking defects by phosphorylation at S129 in yeast
1072 depends on genetic context. Hum Mol Genet. 2012;21:2432–49.

1073 78. Ciaccioli G, Martins A, Rodrigues C, Vieira H, Calado P. A powerful yeast model to
1074 investigate the synergistic interaction of α-synuclein and tau in neurodegeneration. PLoS
1075 One. 2013;8:e55848.

1076 79. Truman AW, Millson SH, Nuttall JM, Mollapour M, Prodromou C, Piper PW. In the yeast
1077 heat shock response, Hsf1-directed induction of Hsp90 facilitates the activation of the Slt2
1078 (Mpk1) mitogen-activated protein kinase required for cell integrity. Eukaryot Cell.
1079 2007;6:744–52.

1080 80. Froula JM, Castellana-Cruz M, Anabtawi NM, Camino JD, Chen SW, Thrasher DR, et al.
1081 Defining α-synuclein species responsible for Parkinson's disease phenotypes in mice. J Biol
1082 Chem. 2019;294:10392–406.

1083 81. Winner B, Jappelli R, Maji SK, Desplats PA, Boyer L, Aigner S, et al. In vivo demonstration
1084 that alpha-synuclein oligomers are toxic. Proc Natl Acad Sci U S A. 2011;108:4194–9.

1085 82. Kayed R, Head E, Thompson JL, McIntire TM, Milton SC, Cotman CW, et al. Common
1086 structure of soluble amyloid oligomers implies common mechanism of pathogenesis.
1087 Science. 2003;300:486–9.

1088 83. Cascella R, Chen SW, Bigi A, Camino JD, Xu CK, Dobson CM, et al. The release of toxic
1089 oligomers from α-synuclein fibrils induces dysfunction in neuronal cells. Nat Commun.
1090 2021;12:1814.

1091 84. Sinnige T, Yu A, Morimoto RI. Challenging Proteostasis: Role of the Chaperone Network
1092 to Control Aggregation-Prone Proteins in Human Disease. In: Mendillo ML, Pincus D,
1093 Scherz-Shouval R, editors. HSF1 and Molecular Chaperones in Biology and Cancer p. 53–
1094 68.

1095 85. Nachman E, Wentink AS, Madiona K, Bousset L, Katsinelos T, Allinson K, et al.
1096 Disassembly of Tau fibrils by the human Hsp70 disaggregation machinery generates small
1097 seeding-competent species. J Biol Chem. 2020;295:9676–90.

1098 86. Saha I, Yuste-Checa P, Da Silva Padilha M, Guo Q, Körner R, Holthusen H, et al. The
1099 AAA+ chaperone VCP disaggregates Tau fibrils and generates aggregate seeds in a cellular
1100 system. Nat Commun. 2023;14:560.

1101 87. Tittelmeier J, Sandhof CA, Ries HM, Druffel-Augustin S, Mogk A, Bukau B, et al. The
1102 HSP110/HSP70 disaggregation system generates spreading-competent toxic α-synuclein
1103 species. The EMBO Journal. 2020;39:e103954.

1104 88. Hall D. On the nature of the optimal form of the holdase-type chaperone stress
1105 response. FEBS Lett. 2020;594:43–66.

1106 89. Macošek J, Mas G, Hiller S. Redefining Molecular Chaperones as Chaotropes. Front Mol
1107 Biosci. 2021;8:683132.

1108 90. Yang S, Huang S, Gaertig MA, Li X-J, Li S. Age-dependent decrease in chaperone activity
1109 impairs MANF expression, leading to Purkinje cell degeneration in inducible SCA17 mice.
1110 Neuron. 2014;81:349–65.

1111 91. Lee YK, Manalo D, Liu AY. Heat shock response, heat shock transcription factor and cell
1112 aging. Biol Signals. 1996;5:180–91.

1113 92. Farkas Z, Kalapis D, Bódi Z, Szamecz B, Daraba A, Almási K, et al. Hsp70-associated
1114 chaperones have a critical role in buffering protein production costs. eLife. 7:e29845.

1115 93. Yaniv Y, Juhaszova M, Sollott SJ. Age-related changes of myocardial ATP supply and
1116 demand mechanisms. Trends Endocrinol Metab. 2013;24:495–505.

1117 94. Gkotsi D, Begum R, Salt T, Lascaratos G, Hogg C, Chau K-Y, et al. Recharging
1118 mitochondrial batteries in old eyes. Near infra-red increases ATP. Exp Eye Res.
1119 2014;122:50–3.

1120 95. de Graff AM, Mosedale DE, Sharp T, Dill KA, Grainger DJ. Proteostasis is adaptive:
1121 Balancing chaperone holdases against foldases. PLoS Comput Biol. 2020;16:e1008460.

1122 96. Tsunemi T, Ishiguro Y, Yoroisaka A, Feng D, Shimada T, Niiyama S, et al. Alpha-synuclein
1123 inhibits the secretion of extracellular vesicles through disruptions in YKT6 lipidation. J
1124 Neurosci. 2025;e2350232024.

1125 97. Gustafsson G, Lööv C, Persson E, Lázaro DF, Takeda S, Bergström J, et al. Secretion and
1126 Uptake of α-Synuclein Via Extracellular Vesicles in Cultured Cells. Cell Mol Neurobiol.
1127 2018;38:1539–50.

1128 98. Gilboa T, Ter-Ovanesyan D, Wang S-C, Whiteman S, Kannarkat GT, Church GM, et al.
1129 Measurement of α-synuclein as protein cargo in plasma extracellular vesicles. Proc Natl
1130 Acad Sci U S A. 2024;121:e2408949121.

1131 99. Zanata SM, Lopes MH, Mercadante AF, Hajj GNM, Chiarini LB, Nomizo R, et al. Stress-
1132 inducible protein 1 is a cell surface ligand for cellular prion that triggers neuroprotection.
1133 EMBO J. 2002;21:3307–16.

1134 100. Lopes MH, Hajj GNM, Muras AG, Mancini GL, Castro RMPS, Ribeiro KCB, et al.
1135 Interaction of Cellular Prion and Stress-Inducible Protein 1 Promotes Neuritogenesis and
1136 Neuroprotection by Distinct Signaling Pathways. J Neurosci. 2005;25:11330–9.

1137 101. Ferreira DG, Temido-Ferreira M, Vicente Miranda H, Batalha VL, Coelho JE, Szegö ÉM,
1138 et al. α-synuclein interacts with PrPC to induce cognitive impairment through mGluR5 and
1139 NMDAR2B. Nat Neurosci. 2017;20:1569–79.

1140 102. Fernández-Bautista N, Fernández-Calvino L, Muñoz A, Toribio R, Mock HP, Castellano
1141 MM. HOP family plays a major role in long-term acquired thermotolerance in Arabidopsis.
1142 Plant Cell Environ. 2018;41:1852–69.

1143 103. Lu J, Zhang S, Ma X, Jia C, Liu Z, Huang C, et al. Structural basis of the interplay
1144 between α-synuclein and Tau in regulating pathological amyloid aggregation. J Biol Chem.
1145 2020;295:7470–80.

1146 104. Lowe R, Pountney DL, Jensen PH, Gai WP, Voelcker NH. Calcium(II) selectively
1147 induces alpha-synuclein annular oligomers via interaction with the C-terminal domain.
1148 Protein Sci. 2004;13:3245–52.

1149 105. Gallardo R, Ranson NA, Radford SE. Amyloid structures: much more than just a cross-
1150 β fold. Curr Opin Struct Biol. 2020;60:7–16.

1151 106. Sawaya MR, Hughes MP, Rodriguez JA, Riek R, Eisenberg DS. The expanding amyloid
1152 family: Structure, stability, function, and pathogenesis. Cell. 2021;184:4857–73.

1153 107. Guerrero-Ferreira R, Kovacik L, Ni D, Stahlberg H. New insights on the structure of
1154 alpha-synuclein fibrils using cryo-electron microscopy. Curr Opin Neurobiol. 2020;61:89–
1155 95.

1156

Main Text Figures

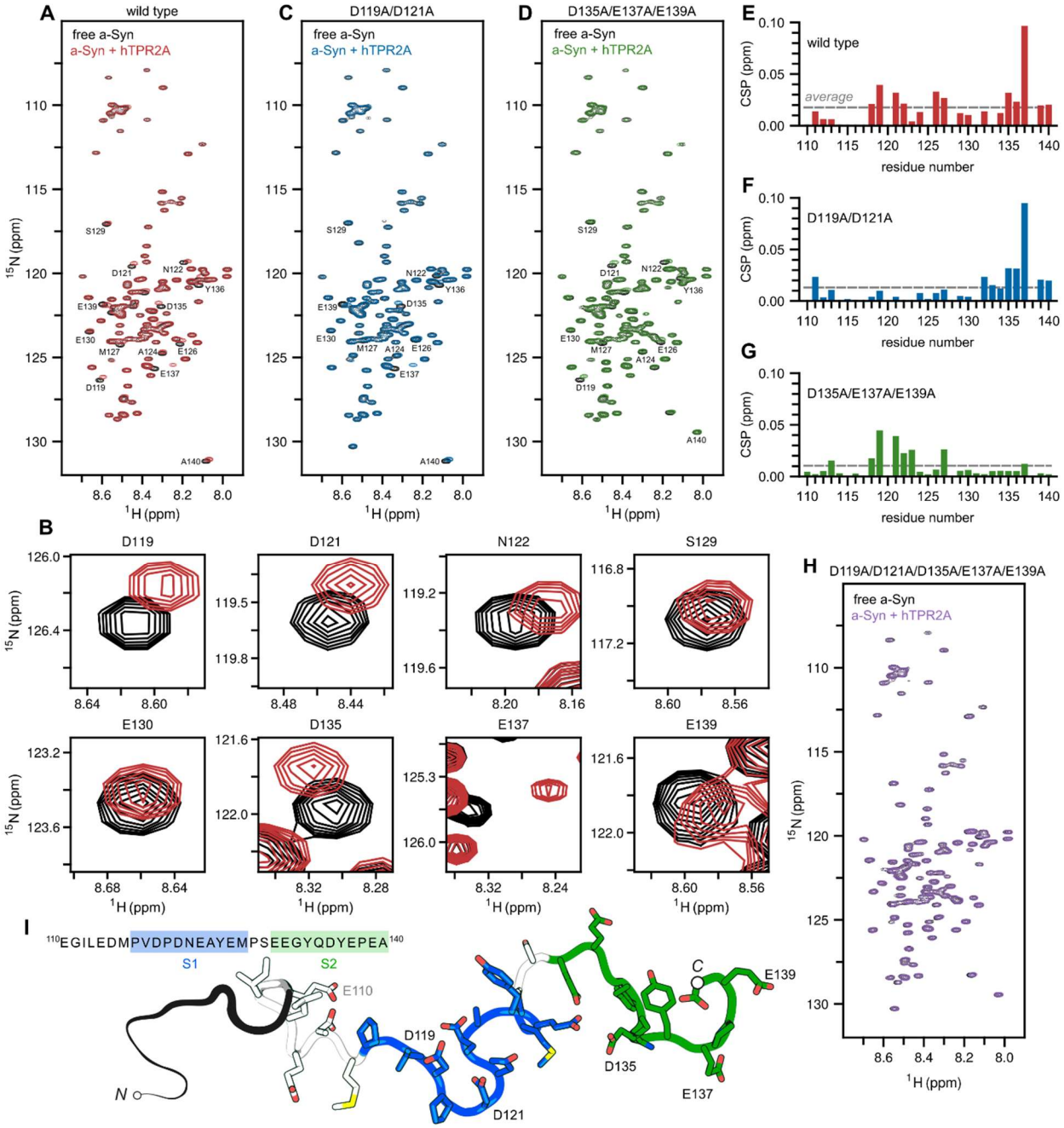

Main Text Figures

Figure 1. Identification of two motifs in the C-terminal of a-Syn which mediate the interaction with TPR2A. (A) NMR analysis of ^{15}N-labeled a-Syn at 100 µM in the absence (black) and the presence of 100 µM hTPR2A (red). (B) Key residues which experience significant chemical shift perturbations upon addition of hTPR2A. (C) ^{1}H-^{15}N HSQC spectrum of 150 µM D119A/D121A a-Syn in the absence (black) and the presence (blue) of 150 µM of hTPR2A. (D) ^{1}H-^{15}N HSQC spectrum of 35 µM D135A/E137A/E139A a-Syn in the absence (black) and the presence (green) of 35 µM of hTPR2A. (E-G) Quantification of chemical shift perturbations (CSPs) observed in the C-terminal domain (residues110-140) of a-Syn (E), D119A/D121A a-Syn (F), and D135A/E137A/E139A a-Syn (G) upon addition of equimolar hTPR2A. The average CSP for the C-terminal residues of each respective a-Syn variant is indicated by dashed line. (H) ^{1}H-^{15}N HSQC spectrum of 35 µM D119A/D121A/D135A/E137A/E139A a-Syn in the absence (black) and the presence (purple) of 35 µM of hTPR2A. (I) Cartoon depiction of the proposed two hTPR2A binding sites in the C-terminal domain of a-Syn, in which site 1 (S1) includes residues D119 and D121, and site 2 (S2) includes residues D135, E137, and E139. Sequences comprising the peptides used for the full C-terminal domain of a-Syn, as well as S1 and S2 individually, are displayed.

Main Text Figures

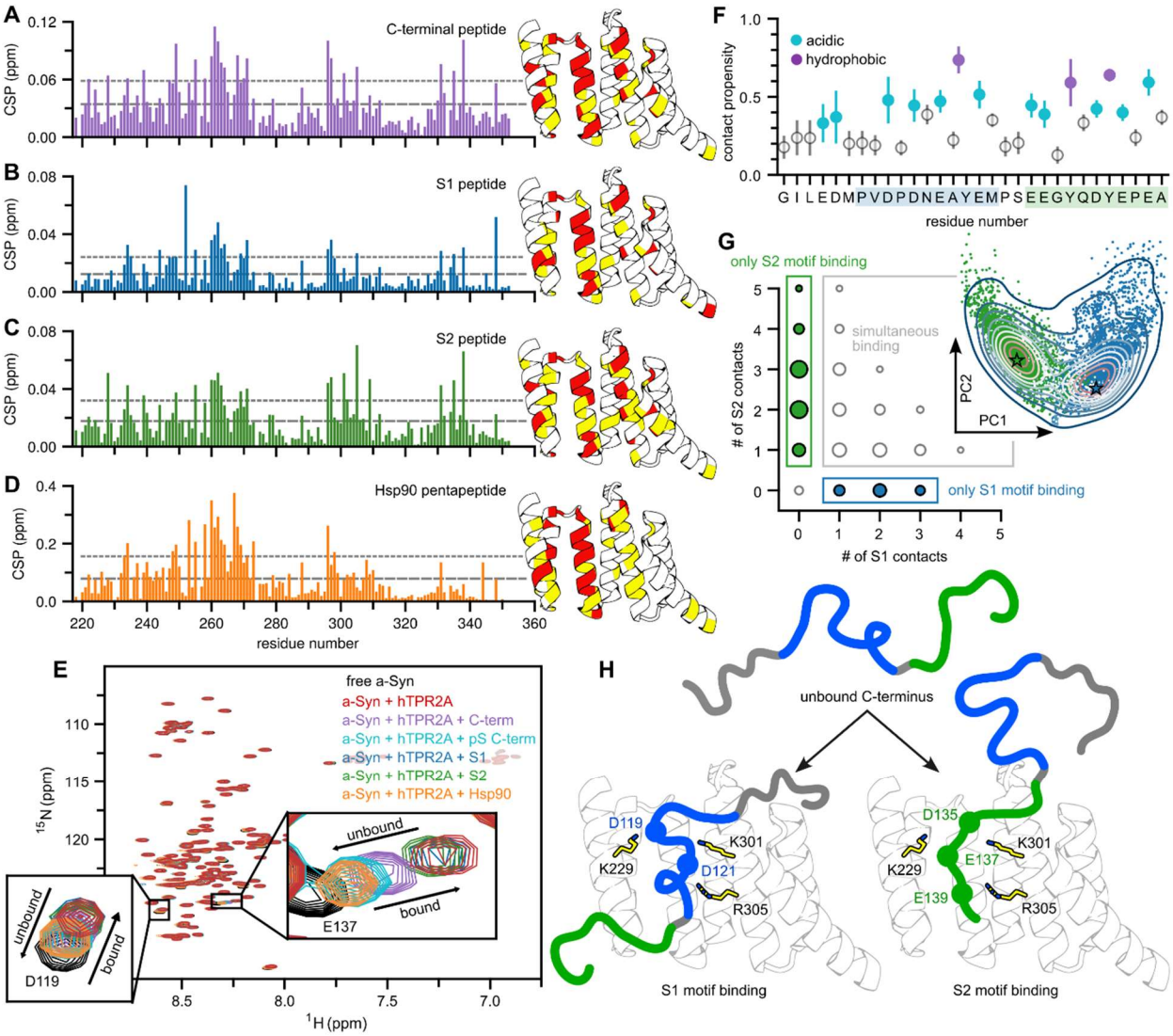

Main Text Figures

Figure 2. Competition for the Hsp90 pentapeptide interface on hTPR2A blocks binding of both S1 and S2 of a-Syn. (A-D) Quantification of chemical shift perturbations (CSPs) observed in residues of 200 μM ^{15}N-labeled hTPR2A upon addition of 400 μM C-terminal a-Syn peptide (A), 800 μM S1 peptide (B), 400 μM S2 peptide (C) and 400 μM Hsp90 pentapeptide (D). Missing bars indicate prolines for which no chemical shift perturbations are measured. The dashed line represents the average CSP value, and the dotted line represents one standard deviation (SD) above the average CSP value. Residues which experience a CSP greater than the average are colored yellow and residues which experience a CSP greater than one SD above the average are colored red on the cartoon of the solved structure of hTPR2A bound to the Hsp90 pentapeptide (PDB:1ELR). (E) NMR competition assay monitoring the chemical shifts of 100 μM ^{15}N-labeled a-Syn (black) in the presence of 100 μM hTPR2A (red) and the transitions between the bound and unbound states upon the addition of 100 μM a-Syn C-terminal peptide (purple), 100μM pS129 a-Syn C-terminal peptide (cyan), 100 μM S1 peptide (blue), 100 μM S2 peptide (green), or 100μM Hsp90 pentapeptide (orange). (F) Analysis of contact propensity for a-Syn residues with any other residues in hTPR2A. Acidic residues are colored cyan and aromatic side chain residues are colored purple. The S1 and S2 motifs are highlighted, in blue and green respectively. (G) The probability histogram of contact configurations between the S1 and S2 motifs and hTPR2A. Residues can form multiple contacts. Circle radius indicates the probability of finding a specific contact configuration e.g., top left marker corresponds to the probability of configurations with 0 S1 contacts and 5 S2 contacts. (G, inset) Electrostatic contact Principal Component Analysis (PCA) projection of all configurations (points) in the simulation ensemble. PC1 captures ~40% of the variance. Points are continuously colored according to whether the configuration mainly involves interactions with S1 (blue), S2 (green), or both motifs (white). (H) Model of the interaction between S1 and S2 of a-Syn with hTPR2A highlighting key electrostatic interactions between S1 and S2 of a-Syn with the Hsp90 interacting residues (K229, K301, and R305) of hTPR2A.

Main Text Figures

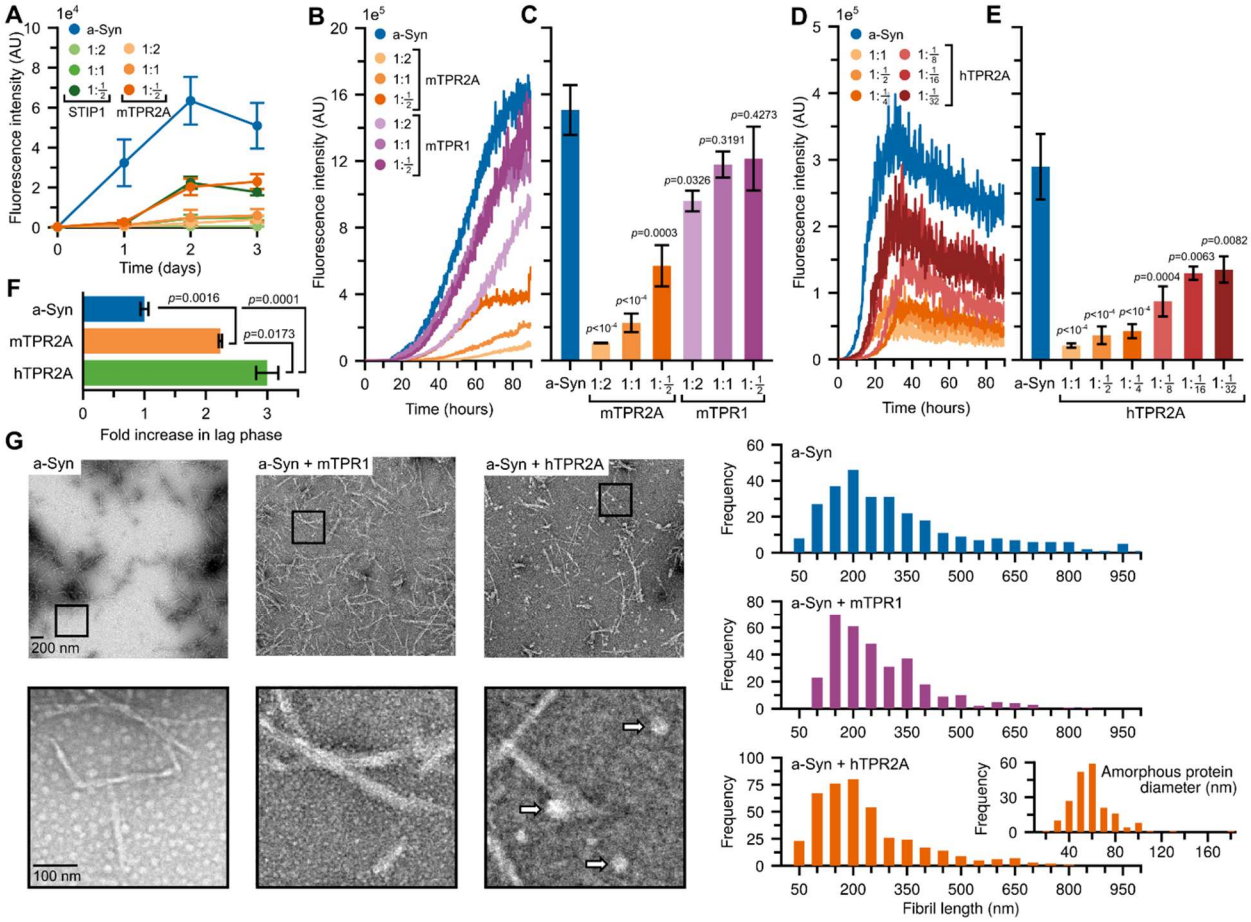

Figure 3. ThT analysis of a-Syn fibril formation in the presence of TPR2A. (A) Fibril formation of a-Syn (20 µM) measured by ThT fluorescence in the absence (blue) or presence of either STIP1 or the TPR2A domain of STIP1 at concentrations ranging from 1/2-fold to 2-fold relative to a-Syn. (B) Fibril formation of a-Syn (60 µM) measured by ThT fluorescence in the presence of mTPR2A or mTPR1 at concentrations ranging from 1/2-fold to 2-fold relative to a-Syn and (C) quantification of final steady-state values. (D) Fibril formation of a-Syn (60 µM) measured by ThT fluorescence in the presence of hTPR2A at concentrations ranging from 1/32-fold to 1-fold relative to a-Syn and (E) quantification of final steady-state values. (F) Comparison of lag phase extension when a-Syn (60 µM) is aggregated in the presence of equimolar mTPR2A or hTPR2A. Error bars represent standard errors of the mean. Statistical significance is in reference to the control condition unless otherwise indicated. (G) Representative EM images at low (upper) and high (lower) magnification taken after 5 days of a-Syn (175 µM) aggregation in the absence or presence of equimolar mTPR1 and hTPR2A with quantification of the distribution of fibril lengths observed and the diameter of the amorphous protein species observed in the presence of hTPR2A (highlighted by white arrows). To determine statistical significance, unpaired t-tests were used to compare means and standard deviations between relevant controls and experimental data sets (n=4). All data are mean ± SEM.

Main Text Figures

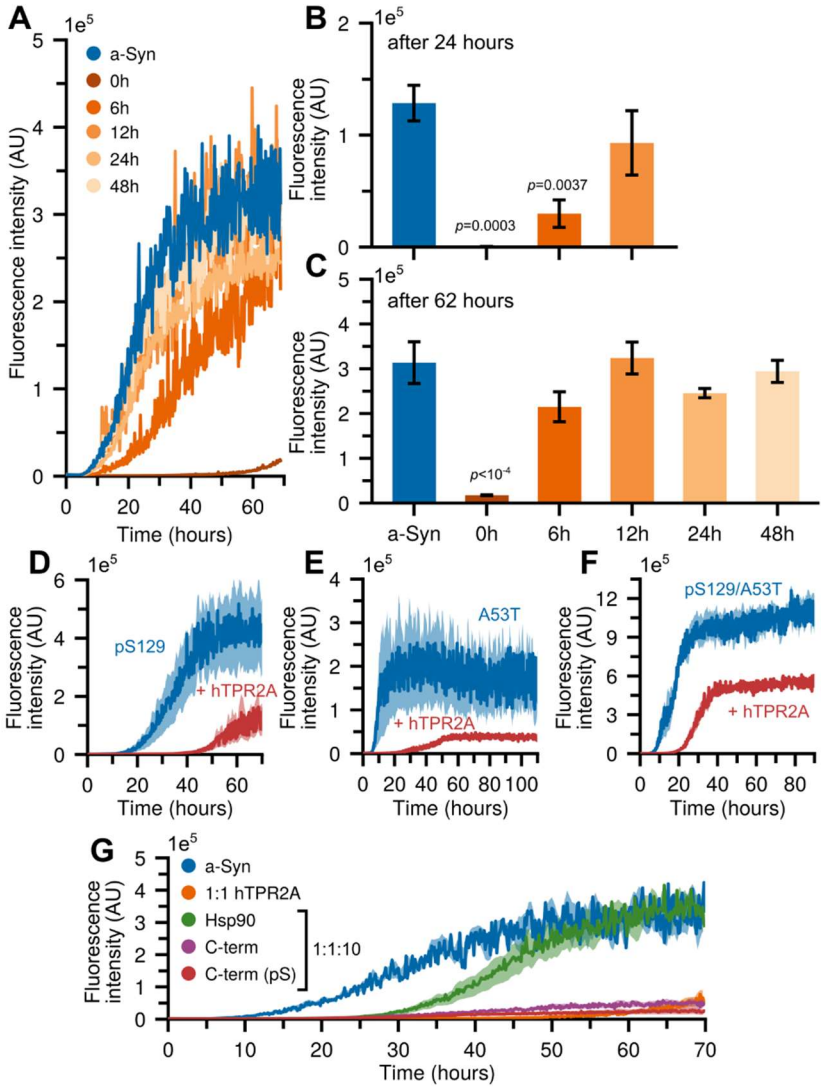

Figure 4. The addition of hTPR2A during early stages of a-Syn aggregation decreases the fibril formation of a-Syn and disease associated a-Syn variants. (A-C) Fibril formation of a-Syn (60 µM) measured by ThT fluorescence in the presence of hTPR2A at equimolar concentrations added at time 0, 6, 12, 24, and 48 hours after starting aggregation (A) and quantification of steady-state values at 24 hours (B) and 62 hours (C) of aggregation. Error bars represent standard errors of the mean. Statistical significance is in reference to the control condition unless otherwise indicated. (D-F) Fibril formation of pS129 a-Syn (D), A53T a-Syn (E), and pS129/A53T a-Syn (F) (60 µM) measured by ThT fluorescence in the presence of hTPR2A at equimolar concentrations. (G) Fibril formation of a-Syn (60 µM) measured by ThT fluorescence in the presence of equimolar hTPR2A and various peptides at a concentration of 10-fold excess of that of a-Syn. To determine statistical significance, unpaired t-tests were used to compare means and standard deviations between relevant controls and experimental data sets (n=4). All data are mean ± SEM.

Main Text Figures

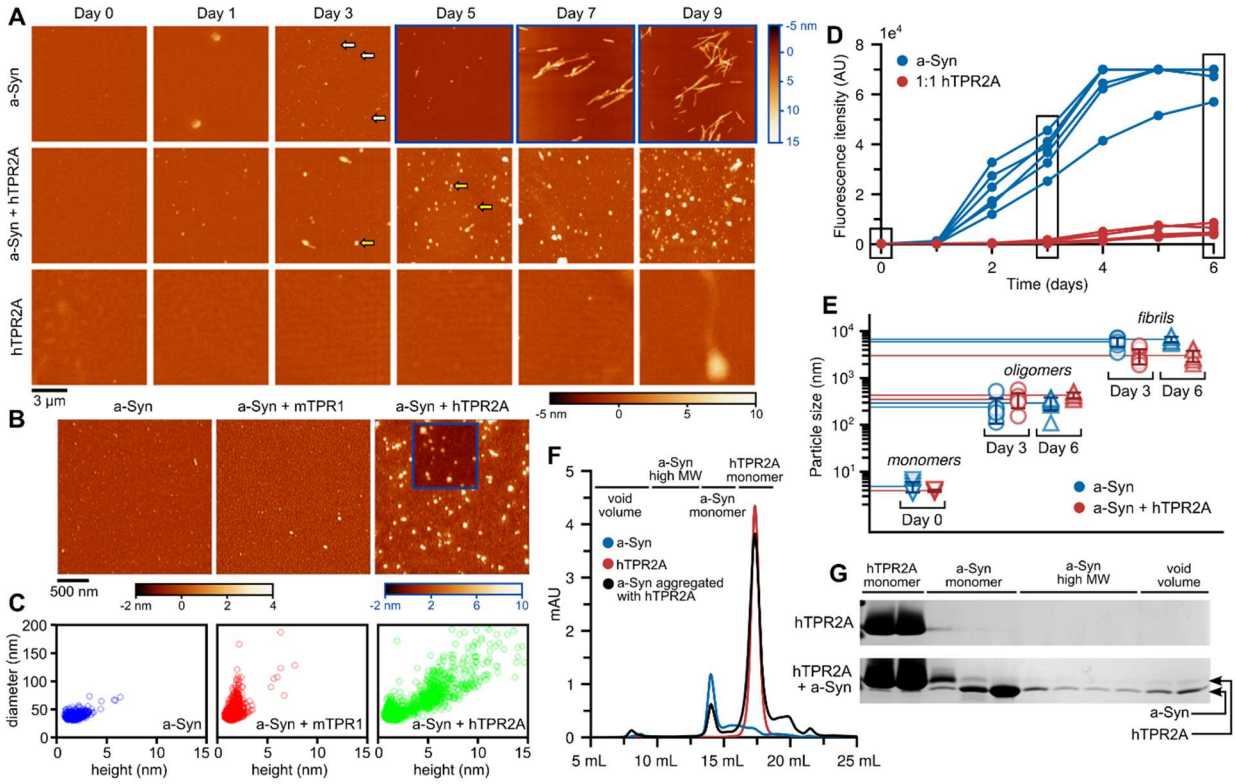

Main Text Figures

Figure 5. hTPR2A promotes the formation of and maintains large amorphous a-Syn species. (A) Representative AFM images of a-Syn aggregation (60 μM) in the absence and presence of and hTPR2A at an equimolar concentration as a function of time. Protein samples are deposited on a mica surface. Scale bar applies to all images. The color map with black font corresponds to all images except those out lined in blue. The color map with blue font corresponds to those images. Grey arrows indicate a-Syn oligomers and yellow arrows indicate what we define here as amorphous high molecular weight aggregates. (B) Representative AFM images of amorphous high molecular weight a-Syn species produced during the aggregation of a-Syn in the absence or presence of mTPR1 and hTPR2A at equimolar concentrations taken on the 3rd day of incubation when the population of a-Syn oligomers was largest. (C) Correlation plots of the distribution of the heights and diameters of the amorphous high molecular weight a-Syn species produced in the absence or presence of mTPR1 and hTPR2A on the 3rd day of incubation. (D) Fibril formation of a-Syn (20 μM) measured by ThT fluorescence in the absence (blue) or presence of equimolar (red) concentration of hTPR2A. Samples were collected after 3 and 6 days of aggregation for further DLS analysis. (E) Quantification of the hydrodynamic radius measured in nm of a-Syn monomers (4 nm), oligomers (100-800 nm), and fibrils (>1,000 nm) after 60 μM a-Syn was aggregated for 3 and 6 days at 37 °C in the absence (blue) or presence of hTPR2A (red), as determined using a DynaPro NanoStar dynamic light scattering instrument (Wyatt Technologies). (F) Chromatographs produced by passing a-Syn (300 μM) (blue), a-Syn with equimolar hTPR2A (black), or hTPR2A alone (red) that was incubated at 37 °C for 48 hours through a Superdex Increase 200 size exclusion column. Peaks corresponding to the location of monomeric hTPR2A, monomeric a-Syn, and high molecular weight oligomeric a-Syn species bound to hTPR2A are labeled on the chromatograph. (G) SDS-PAGE gel of fractions collected from the Superdex Increase 200 size exclusion column demonstrating the change in the fractionation of hTPR2A.

Main Text Figures

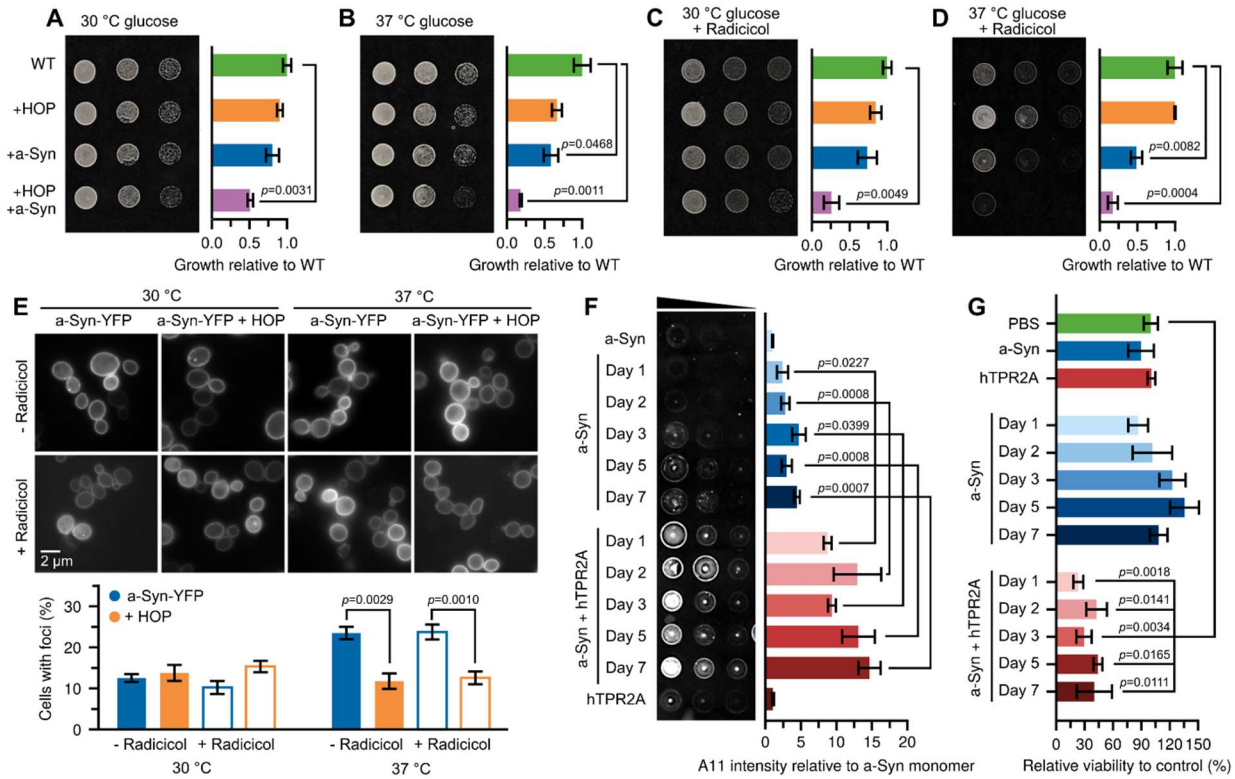

Figure 6. hTPR2A promotes amorphous oligomer-like a-Syn species and increases the toxicity of a-Syn. (A-D) Spotting assay of wildtype (BY4741) yeast expressing a control plasmid, HOP, a-Syn, or expressing HOP and a-Syn grown at optimal growth temperatures (30 °C) (A, C) or under heat stress conditions (37 °C) (B, D) on SD media in the absence (A, B) or presence of Radicicol (C, D). (E) Upper: Fluorescence microscopy of yeast (BY4741) cells expressing a-Syn-YFP or co-expressing both a-Syn-YFP and HOP grown under optimal and heat stress growth temperatures in the absence and presence of Radicicol. Lower: Quantification of a-Syn cytoplasmic foci observed under each condition. (F) Samples of a-Syn aggregated in the absence or presence of equimolar hTPR2A from subsequent timepoints were spotted in three five-fold dilutions from left to right and examined by dot blotting analysis using the anti-oligomer antibody A11. The quantitative analysis of the A11 signal relative to monomeric a-Syn was performed for 3 independent aggregation reactions of each mixture. (G) Quantification of cell viability measured from SH-SY5Y cells after treatment with 35 µM of a-Syn aggregated in the absence or presence of equimolar hTPR2A for subsequent time periods and control samples of monomeric a-Syn, hTPR2A and PBS buffer. To determine statistical significance, unpaired t-tests were used to compare means and standard deviations between relevant controls and experimental data sets (n=3). All data are mean ± SEM.

Main Text Figures

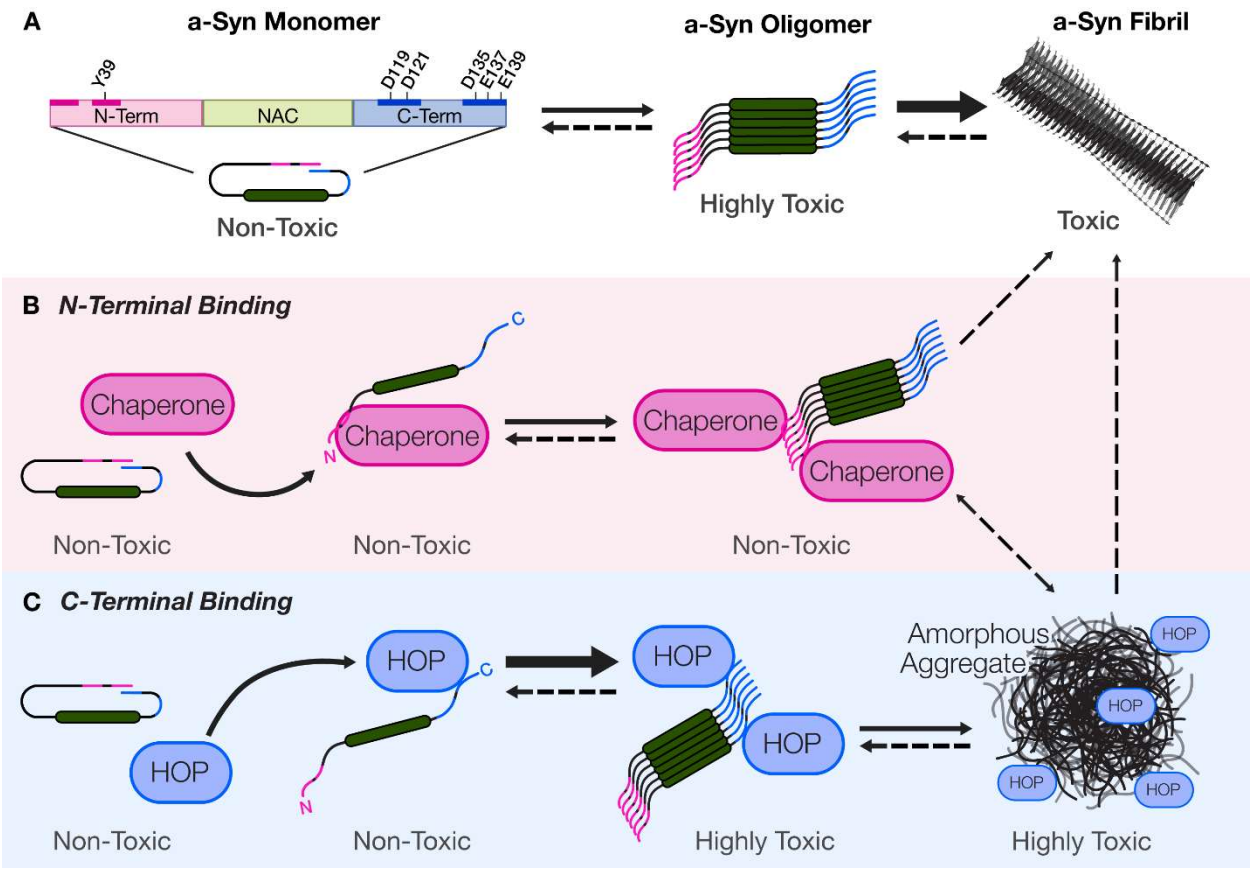

Figure 7. Protein interactions with the N- and C-terminal domains of a-Syn modulate aggregation and toxicity. (A) Intramolecular interactions between the terminal domains of monomeric a-Syn provide an energetic barrier to oligomer formation and favor fibril formation. (B) Molecular chaperones recognize and bind hydrophobic motifs (pink) in the N-terminal domain, maintain monomeric a-Syn conformers and masking the toxicity of oligomers. (C) HOP interacts with motifs of charged residues (blue) in the C-terminal domain of a-syn, promoting the formation of toxic amorphous aggregates.